Solution Structure of the Mithramycin Dimer–DNA Complex†

Mallika Sastry‡ and Dinshaw J. Patel*,‡,§

Department of Biochemistry and Molecular Biophysics, College of Physicians and Surgeons, Columbia University, New York, New York 10032, and Cellular Biochemistry and Biophysics Program, Memorial Sloan-Kettering Cancer Center, 1275 York Avenue, New York, New York 10021

Received January 6, 1993; Revised Manuscript Received April 8, 1993

ABSTRACT: We have characterized the NMR parameters for the complexes formed by the Mg^{2+}-coordinated mithramycin dimer with self-complementary d(T-G-G-C-C-A) and d(T-C-G-C-G-A) duplexes. The solution structure of the latter complex has been determined using a combined NMR–molecular dynamics study including relaxation matrix refinement. The Mg^{2+}-coordinated mithramycin dimer–d(T-C-G-C-G-A) complex exhibits a 2-fold center of symmetry with the divalent cation coordinated aglycons positioned opposite the central (G3-C4)·(G3-C4) segment such that the aglycon C^8 hydroxyl oxygens form symmetrical sequence-specific hydrogen bonds to guanine amino protons in the complex. The C-D-E trisaccharide segments of each monomer in the mithramycin dimer adopt extended conformations, are positioned inside the minor groove, and are directed toward either end of the duplex. The C-D saccharide component of one monomer and the aglycon of the other monomer in the mithramycin dimer share a widened minor groove with the hydrophobic edges of the C and D sugars interacting with individual strands of the duplex. The E-sugar ring is positioned in the floor of the minor groove, and its hydroxyl-bearing face interacts with both strands of the duplex through hydrogen-bonding and hydrophobic intermolecular interactions. The A-B disaccharide and the hydrophilic side chain form intermolecular contacts with the sugar–phosphate backbone in the complex. The antiparallel alignment of divalent cation coordinated monomers in the mithramycin dimer results in the two outwardly directed C-D-E trisaccharide segments generating a right-handed continuous hexasaccharide domain that spans six base pairs in the minor groove of the duplex. The solution structure of the mithramycin dimer–DNA complex reported in this study and the solution structure of the chromomycin dimer–DNA complex reported previously [Gao, X., Mirau, P., & Patel, D. J. (1992) *J. Mol. Biol. 223,* 259–279] show global similarities, as well as local differences that are of interest. All four nucleotides in the tetranucleotide segment of the duplex centered about the sequence-specific (G-C)·(G-C) step adopt A-DNA sugar puckers and glycosidic torsion angles in the chromomycin dimer–DNA complex, while only the central cytidine adopts an A-DNA sugar pucker and glycosidic torsion angle in the mithramycin dimer–DNA complex. Further, differences in both the hydrogen bonding and the hydrophobic nature of the substituents on the E-sugar face positioned in the floor of the minor groove result in reduced sequence selectivity for mithramycin dimer–DNA complexes relative to chromomycin dimer–DNA complexes. These high-resolution solution structural studies provide plausible explanations for modulations in the sequence selectivity within the aureolic acid family of antitumor drug dimers for their DNA target sites.

The isolation of aureolic acid, a yellow crystalline compound, from three strains of streptomyces species was reported in 1953 (Grundy et al., 1953; Philip & Schenck, 1953). Subsequently the isolation and preliminary structural characterization of chromomycin A3 (Chr, **1**), mithramycin A (Mth, **2**), and olivomycin, which belong to the aureolic acid group of antibiotics, was reported (Berlin et al., 1966; Miyamoto et al., 1964; Bakhaeva et al., 1968) (Chart I). The complete chemical structures of chromomycin, mithramycin, and olivomycin have since been elucidated (Miyamoto et al., 1964; Thiem & Meyer, 1981; Ramakrishna et al., 1990). All three antitumor agents contain an aglycon chromophore and five 2,6-dideoxy hexopyranoses. Mithramycin and the related antitumor agents are effective against a wide variety of experimental and human tumors (Kennedy et al., 1966, 1968). Mithramycin has also been used in the treatment of Paget's disease of bone (Elias & Evans, 1970). Mithramycin acts by inhibiting DNA-dependent RNA synthesis by binding to template DNA only in the presence of stoichiometric amounts of Mg^{2+} ions (Wakasaki et al., 1963; Ward et al., 1965). All three members of the aureolic acid group display a preference for guanine-rich DNA sequences. Miller et al. have shown that mithramycin prevents protein binding to G·C-rich regulatory regions of the SV40 and c-*myc* promoters (Ray et al., 1989; Miller et al., 1989). Furthermore, mithramycin also inhibits RNA synthesis when the template DNA consists of alternating 2,6-diamino purine and thymine residues, thus indicating that the amino group of guanine is critical for binding (Cerami et al., 1967).

Chemical (van Dyke & Dervan, 1983; Cons & Fox, 1989a,b; Stankus et al., 1992) and DNase I (Fox & Howarth, 1985) footprinting studies on mithramycin–DNA and chromomycin–DNA complexes show that these drugs prefer guanine-rich sequences. These two antitumor agents exhibit similar sequence specificities, with the binding site being nearly three base pairs long and containing at least two contiguous G·C base pairs (van Dyke & Dervan, 1983). Hydroxyl radical footprinting studies showed that, although two contiguous

† This research was supported by NIH Grant CA-46778 to D.P. The NMR spectrometers were purchased from funds donated by the Robert Woods Johnson Jr. Trust and the Matheson Trust toward setting up the NMR Center in the Basic Medical Sciences at Columbia University. We acknowledge the use of the Molecular Modeling Facility for Molecular Biology at Columbia University, supported in part by NSF Grant DIR-8720229.

‡ Columbia University.

§ Memorial Sloan-Kettering Cancer Center.

0006-2960/93/0432-6588$04.00/0

Chart I

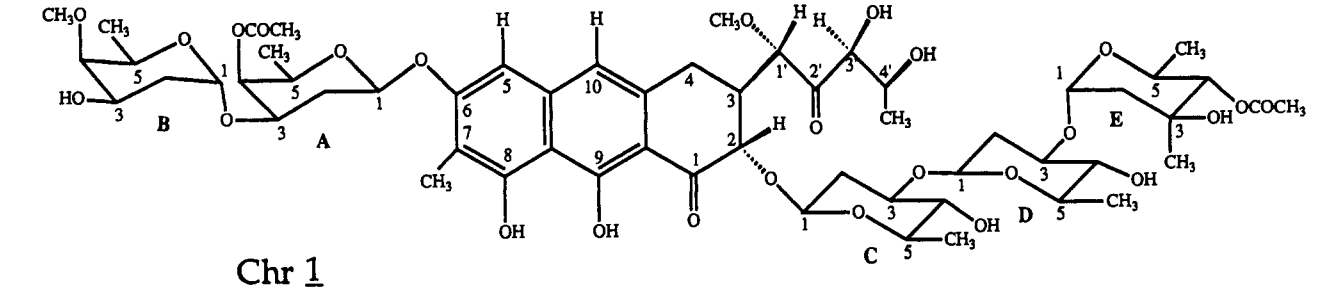

Chr 1

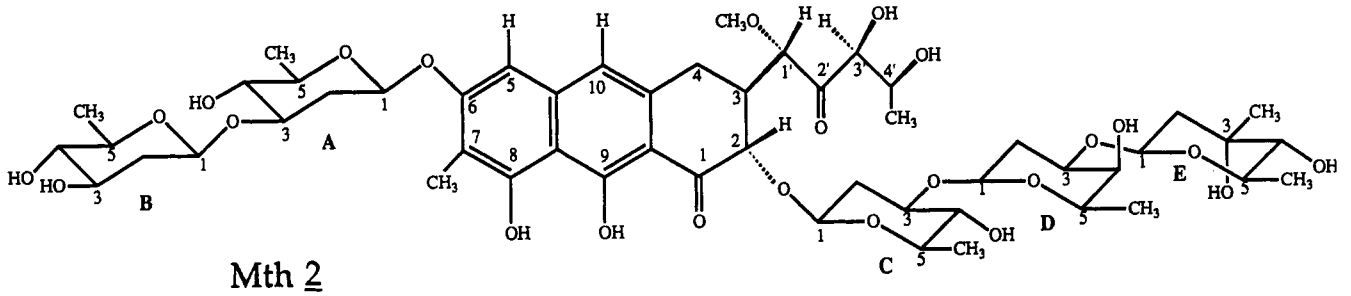

Mth 2

G·C base pairs could constitute a good binding site, the best sites contained three contiguous G·C base pairs. However, in these studies all such sites were not protected, indicating that the flanking sequences play a role in binding (Cons & Fox, 1990). Footprinting studies also indicated that mithramycin binding renders adjacent $(A\cdot T)_n$ sequences sensitive to attack by DNAse II (Cons & Fox, 1990, 1991).

The first insights into the structure and dynamics of aureolic acid antitumor agent–DNA oligomer complexes have emerged from high-resolution NMR studies on the chromomycin–d(T-T-G-G-C-C-A-A) complex in Mg^{2+}-containing aqueous solution (Gao & Patel, 1989a,b). This research established that chromomycin bound as a Mg^{2+}-coordinated head-to-tail dimer to a widened and shallower minor groove of the central (G-G-C-C)·(G-G-C-C) segment of the duplex. The hydrophilic edge of each aglycon chromophore was located next to the (G-G)·(C-C) half-site, and each C-D-E trisaccharide chain extended toward the 3′-end of the octanucleotide duplex. The initial low-resolution structure of the chromomycin dimer–DNA complex (Gao & Patel, 1989a) was subsequently refined using a relaxation matrix analysis of the two-dimensional NOESY data sets (Gao et al., 1992). The sequence specificity of the chromomycin dimer for G·C-rich segments was associated with specific intermolecular hydrogen bonds between the OH group of C^8 of the aglycon chromophore and the minor groove guanine NH_2 and N^3 groups of the central (G-C)·(G-C) segment (Gao & Patel, 1989a; Gao et al., 1992). The solution structure of the complex also established that saccharide–minor groove interactions provide important recognition and stabilization elements.

The divalent cation coordination site on the chromomycin dimer in the complex was elucidated from systematic studies using diamagnetic Mg^{2+}, Zn^{2+}, and Cd^{2+} cations, as well as paramagnetic Ni^{2+} and Co^{2+} cations (Gao & Patel, 1990). These studies established that the O^2 carbonyl and ionized O^9 enolate anion on the hydrophilic edge of each aglycon chromophore is coordinated to the divalent cation in the complex. Both the stability of the complex and the kinetics of the divalent cation exchange were found to be dependent on the nature of the bound divalent cation in the complex (Gao & Patel, 1990). These structural studies have been complemented by hydrogen-exchange measurements at the individual base pair level on chromomycin dimer–DNA oligomer complexes (Leroy et al., 1991). The base pair opening lifetimes were found to be an order of magnitude longer at the G·C-rich chromomycin dimer binding sites in the complex.

Our demonstration that chromomycin bound as a divalent cation coordinated head-to-tail dimer to the minor groove of the DNA duplex (Gao & Patel, 1989a; Gao et al., 1992) ruled out earlier NMR-based models that claimed that chromomycin intercalated as a monomer into synthetic DNAs (Berman et al., 1985) and that chromomycin bound as a monomer to the major groove of DNA oligomer duplexes (Keniry et al., 1987). These unsubstantiated structural claims (Berman et al., 1985; Keniry et al., 1987) have been subsequently withdrawn (Banville et al., 1990a) following publication of the chromomycin dimer–DNA results from our laboratory (Gao et al., 1989a).

We have now extended our NMR structural studies on chromomycin dimer–DNA oligomer complexes (Gao & Patel, 1989a, 1990; Gao et al., 1992; Leroy et al., 1991) to those complexes formed between the related antibiotic mithramycin and its DNA binding sites. There are several differences between the two antibiotics, including functional groups on the sugar rings, sugar chirality, and sugar–sugar linkages. Thus, chromomycin (Chr), **1**, and mithramycin (Mth), **2** differ at the A-B and D-E sugar–sugar linkages, as well as in the chirality of the E sugar. These differences between the two antibiotics could modulate the sequence specificity of complex formation at the DNA duplex level. We report below on a combined NMR and molecular dynamics computational study including relaxation matrix refinement that defines the solution conformation of the mithramycin dimer–d(T-C-G-C-G-A) complex in Mg^{2+}-containing aqueous solution.

MATERIAL AND METHODS

Oligonucleotide Synthesis. The self-complementary hexanucleotides d(T-C-G-C-G-A), **3**, and d(T-G-G-C-C-A), **4**, were synthesized on the 10-μmol scale on an Applied Biosystems Model 391 synthesizer using cyanoethyl phosphoramidite chemistry. The crude 5′-dimethoxytritylated oligonucleotide was isolated by treatment of the support with concentrated aqueous ammonia for 48 h at room temperature. The products were purified by reverse-phase HPLC in two stages followed by desalting on a Sephadex G-25 column. The

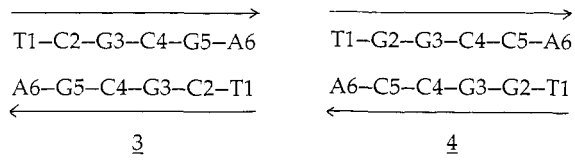

oligonucleotide was finally converted to the sodium form by using a Dowex cation-exchange resin column.

Mithramycin–Oligonucleotide Complex. Mithramycin was a gift from Pfizer, Inc., while $MgCl_2 \cdot 6H_2O$ was purchased from Aldrich. The complex between mithramycin and the d(T-C-G-C-G-A) duplex was generated either by addition of 3-μL aliquots of a $MgCl_2 \cdot 6H_2O$ (0.15 μmol/μL) solution to an aqueous solution of 2:1 mithramycin/duplex or by addition of solid mithramycin to duplex in Mg^{2+}-containing buffer (0.1 mM EDTA, 10 mM $Na_2HPO_4 \cdot 7H_2O$, 0.1 M NaCl, and 7.5 mM $MgCl_2 \cdot 6H_2O$). Complex formation was monitored by one-dimensional proton NMR. The titration was followed by monitoring peak intensities of free duplex and complex and was complete when the ratio of drug to duplex to Mg^{2+} equaled 2:1:1 equivalents.

NMR Experiments. One- and two-dimensional proton NMR experiments were recorded with quadrature detection at either 400 or 500 MHz on Bruker AM 400 and AM 500 spectrometers. Two-dimensional data sets were processed by using FTNMR software (Hare Research).

Two-dimensional phase-sensitive NOESY spectra (170-ms mixing time) in H_2O buffer were recorded using a 70° preparation and mixing pulses combined with a jump and return pulse sequence (Plateau & Gueron, 1982) for the detection pulse. The carrier frequency was set on the H_2O resonance, and the waiting time, t, was 40 or 68.3 μs such that maximum excitation was obtained at 16 or 12 ppm for the complex or the free duplex, respectively. The time domain data sets consist of 1024 complex data points with a spectral width of 23.8 ppm in t_2. The residual H_2O signal was further reduced by using the time domain convolution method of Marion et al. (Marion et al., 1989).

Two-dimensional phase-sensitive NOESY (States et al., 1982) spectra were also recorded in D_2O with the carrier frequency positioned on the residual HDO signal. Sixty-four scans were collected for each of the 256 t_1 increments with a repetition delay of 1.2–1.8 s. A spectral width of 9–10 ppm was used to collect 1024 complex data points in t_2. The decoupler channel was used to suppress the residual HDO signal. The free induction decays in t_2 and t_1 were apodized with a sine bell function.

Correlated spectra (DQF-COSY, COSY-45) were recorded in the phase-sensitive mode (States et al., 1982) in D_2O solution. Time domain data sets were collected with a spectral width of 8–10 ppm by using 1024 (DQF-COSY) and 2048 (COSY-45) complex data points in the t_2 dimension and 256 t_1 increments. Data sets were apodized with a sine bell window function along t_2 and t_1. The free induction decay was zero-filled to 2048 points after apodization in the t_1 dimension for the COSY-45 experiment.

Phase-sensitive two-dimensional proton-detected proton–phosphorus correlation spectra (Sklenar & Bax, 1987) were recorded on a 5-mm proton inverse probe on a Varian 400-MHz spectrometer. A hard loop was used in the beginning of the sequence to saturate the protons, and a delay of 10 ms was used before restarting the sequence. For the two-dimensional data sets 128–256 scans were collected for each of the 128 t_1 increments. Spectral widths of 4000 Hz in t_2 and 1620 Hz in t_1 were used. The two-dimensional data sets were processed using FELIX and VNMR software. Chemical shifts along t_1 were referenced to trimethyl phosphate in D_2O. Two-dimensional homonuclear Hartmann–Hahn (HOHA-HA) spectra were recorded in D_2O solution with a 68-ms spin-lock time. Time domain data sets were accumulated over a spectral width of 10 ppm by using 1024 and 256 complex data points in t_2 and t_1, respectively. The free induction decays were apodized with a sine bell function in both the t_2 and t_1 dimensions prior to Fourier transformation.

Buildup Experiments. Two-dimensional phase-sensitive (States et al., 1982) NOESY experiments were recorded in D_2O with mixing time values of 50, 80, 100, 150, 200, and 250 ms at 25 °C. The FIDs in t_2 and t_1 were apodized with a 90° shifted sine bell function and baseline corrected using a polynomial baseline fitting routine in t_2 and t_1.

Interproton Distance Constraints. For each resolved NOE cross peak in the NOESY spectrum of the complex we measured a buildup of intensity as a function of mixing times. The interproton distance between two protons was estimated on the basis of the slope of the linear portion of the buildup curves obtained by plotting intensities vs mixing time, τ_m. The cytidine H5–H6 distance of 2.48 Å was used as the standard for interproton distances involving the nucleic acid protons. A distance of 2.41 Å for H5–H10 protons of the aglycon was used as a standard for calculating interproton distances involving the mithramycin protons. Each of these distances was given an upper and a lower bound. A larger upper bound was given to NOE-derived distances involving methyl protons. For the mithramycin dimer–d(T-C-G-C-G-A) complex, the observed NOEs include intramolecular nucleic acid constraints, intramolecular mithramycin dimer constraints, and intermolecular constraints. Of the 78 intermolecular constraints, 48 constraints could be assigned unambiguously and were used for the distance-restrained molecular dynamics. The remaining constraints were introduced during relaxation matrix refinement as overlap volumes. Of the intramolecular constraints observed, 166 distances for the nucleic acid and 174 distances for the mithramycin dimer were used during distance-restrained molecular dynamics. During relaxation matrix refinement, 216 constraints for the nucleic acid and 298 constraints for the mithramycin dimer were used.

The Mg^{2+}-to-oxygen distances at the divalent cation coordination site were obtained from the crystal structure of Mg^{2+}-coordinated chromomycin dimer–d($T^{Br}UG_2C_2A_2$) complex (C. Ogata, X. Gao, and W. Hendrickson, personal communication). The Mg–O^9 distance was incorporated as a covalent bond with a force constant of 20 kcal/(mol·Å^2) and a distance of 1.90 Å as compared with a force constant of 450 kcal/(mol·Å^2) for a C–H bond. The Mg–O^1 distance of 2.05 Å was incorporated in the NOE force field with a weight of 80 kcal/(mol·Å^2) throughout the refinement. An interresidue bond angle of 180° with a force constant of 25 kcal/(mol·rad^2) was defined for the O^9–Mg–O^9 angle. Explicit water molecules and dihedral angles around the Mg^{2+} coordination site were not included in our calculations.

Molecular Dynamics Simulation. Mithramycin (Mth), **2**, was generated using Macromodel (W. C. Still, Columbia University). The self-complementary d(T-C-G-C-G-A) hexanucleotide duplex was generated using Quanta (Polygen Corporation). The starting structure of the mithramycin dimer for docking onto the DNA helix was constructed by satisfying the observed NOE-based distance constraints between drug protons and, in addition, was guided by the known structure of the related chromomycin dimer in its DNA complex (Gao & Patel, 1989a; Gao et al., 1992). Each C-D-E trisaccharide

segment adopts an extended conformation, the Mg^{2+} is coordinated to the O^1 carbonyl and O^9 enolate atoms of each aglycon, and the monomers are aligned in a head-to-tail orientation, in this starting structure of the Mg^{2+}-coordinated mithramycin dimer. Two different starting structures were used to obtain the distance-refined structures of the Mth dimer–d(T-C-G-C-G-A) complex, one with mithramycin dimer docked onto the minor groove of A-form DNA and another with mithramycin dimer docked onto the minor groove of B-form DNA. Alignment of the mithramycin dimer in the minor groove was done such that the initial model was compatiable with the observed experimental intermolecular NOE patterns in the complex. Initially one molecule of mithramycin was docked onto the minor groove of the duplex such that it satisfied the experimental NOE constraints. This half-complex containing one molecule of mithramycin was duplicated, rotated by 180°, and superpositioned. The extra duplex was then deleted, giving a Mg^{2+}-coordinated mithramycin dimer in the minor groove of the d(T-C-G-C-G-A) duplex.

Restrained molecular dynamics on the Mth dimer–d(T-C-G-C-G-A) complex was carried out using algorithms implemented in the program X-PLOR, version 2.1 (A. Brunger, Yale University), on a Convex C2 computer. The SHAKE algorithm (Brooks et al., 1983) was used to constrain bond lengths involving hydrogens during the molecular dynamics simulation. The solvent electrostatic effect was simulated by a distance-dependent dielectric and a dielectric constant of 80. A switched van der Waals function was used to reduce the van der Waals potential to 0 at a distance of 7.5–8.0 Å. The hydrogen-bonding potentials were switched off at a distance of 5.5–6.5 Å and a bond angle of 50–70°. Nucleic acid parameters and force constants available in the X-PLOR program were used for the molecular dynamics simulations. The parameters for dideoxy pyranoses in mithramycin were deduced from the values reported for glucose (Brady, 1988) and from the sugar topology and parameters files toph1.cho and paramh1.cho of X-PLOR, version 2.1. For the aglycon of mithramycin, parameters were deduced from the protein parameter file param19x.pro in X-PLOR, version 2.1. Distance constraints derived from experimental NOE data were included in the NOE energy term using a square well function. The 2-fold symmetry of the complex was maintained by applying the noncrystallographic symmetric function in X-PLOR during the entire refinement protocol.

In order to relieve unfavorable van der Waals contacts between nonbonded atoms, each of the initial structures for the complex was subjected to energy minimization using the repel energy function in X-PLOR followed by energy minimization using Lennard-Jones potentials. These structures were further minimized for 50–100 cycles before molecular dynamics simulation. The molecular dynamics simulation with temperature coupling was then initiated by assigning initial velocities to a Maxwell distribution at 1000 K. The scaling factor for NOE-derived proton–proton distances was increased from 0.125 to 8 kcal/(mol·Å^2) during the first 6 ps of molecular dynamics (0.5-fs time step). Another 5.5 ps of molecular dynamics was done with the NOE scaling factor at 8.0 kcal/(mol·Å^2). This was followed by slow cooling to 300 K, 5 ps (1-fs time step) of distance-restrained molecular dynamics at 300 K, and 300 steps of energy minimization to give the distance-restrained structures, DR-A and DR-B. Structure analysis was done on a Silicon Graphics IRIS workstation using the graphics program INSIGHT-II (BIOSYM).

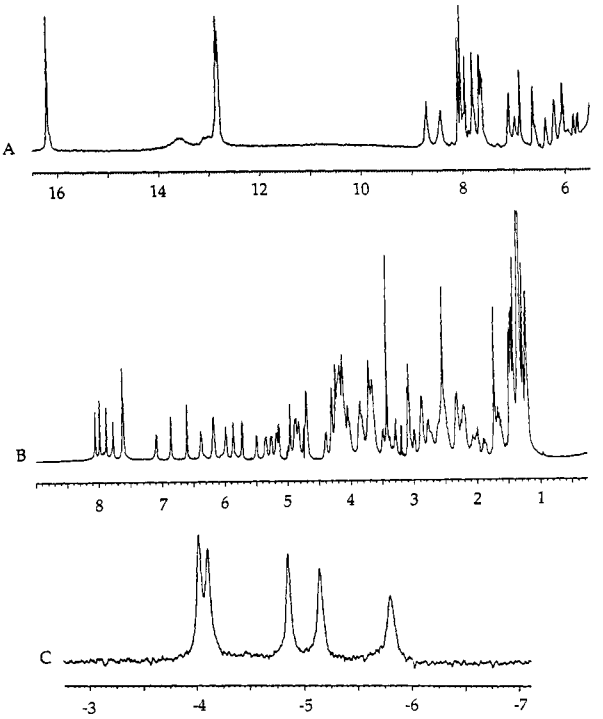

FIGURE 1: NMR spectra of the Mth dimer–d(T-C-G-C-G-A) complex in Mg^{2+}-containing aqueous buffer (0.1 M NaCl, 10 mM $Na_2HPO_4.7H_2O$, 0.1 mM EDTA, and 7.5 mM $MgCl_2.6H_2O$), pH 6.5. (A) Exchangeable proton spectrum (5.5–16.5 ppm) in H_2O buffer at 18 °C. (B) Nonexchangeable proton spectrum (0.3–9.0 ppm) in D_2O buffer at 25 °C. (C) Proton decoupled phosphorus spectrum (–2.75 to –7.1 ppm) in D_2O buffer at 25 °C.

Relaxation Matrix Refinement. NOE relaxation matrix refinement was done with the RELAX routine of the program X-PLOR, version 2.1. The RELAX energy function is based on the full relaxation matrix calculation of NOESY cross-peak volumes (Yip & Case, 1989; Nilges et al., 1991; Shapiro et al., 1992). The distance-refined structures DR-A and DR-B were subjected to 1 ps (1-fs time step) of molecular dynamics at 1000 K during which the scaling factor on the NOE energy term was reduced from 8 to ~0.0001 kcal/(mol·Å^2), while the scaling factor on the RELAX energy function was increased from 5 to 120 kcal/mol. We used a cutoff distance of 4.5 Å during the relaxation matrix refinement. This was followed by slow cooling to 300 K and 2.5 ps of molecular dynamics (1-fs time step) at 300 K. The coordinates for the last 1 ps of dynamics were averaged and subjected to 200 steps of energy minimization. *R* factors were calculated as the weighted average of the absolute value of the difference between observed and calculated intensities (Shapiro et al., 1992).

RESULTS

Mithramycin–d(T-C-G-C-G-A) Complex. The exchangeable proton, nonexchangeable proton, and proton decoupled phosphorus spectra of the Mg^{2+}-coordinated Mth dimer–d(T-C-G-C-G-A) complex are plotted in panels A, B, and C, respectively, of Figure 1. The mithramycin:duplex:Mg^{2+} ratio was 2:1:1. The observation of a single phenolic hydroxyl proton at 16.1 ppm (Figure 1A) and five phosphorus resonances (Figure 1C) establishes that the 2-fold symmetry of the d(T-C-G-C-G-A) duplex is retained on complex formation.

Nucleic Acid Exchangeable Proton Assignments in the Complex. The exchangeable proton NMR spectrum of the Mg^{2+}-coordinated Mth dimer–d(T-C-G-C-G-A) complex in H_2O buffer, pH 6.5 at 18 °C, is plotted in Figure 1A. A

Table I: Proton Chemical Shifts (ppm) in the Mg^{2+}-Coordinated Mth Dimer–d(T-C-G-C-G-A) Complex[a]

d(T-C-G-C-G-A) Protons											
residue	NH	NH_2b,e	H8	H6	H2	H5/CH_3	H1′	H2′	H2″	H3′	H4′
T1	13.63[b]			7.59		1.67	5.91	2.28	2.52	4.66	4.08
C2		8.61, 6.88		7.59		5.67	5.82	2.18	2.53	4.79	4.14
G3	12.80	7.70, 5.87	7.85				6.14	2.68	2.84	4.85	4.27
C4		8.38, 6.54		7.06		5.11	5.46	1.58	1.35	4.21	1.31
G5	12.75		7.74				6.15	2.43	2.85	4.83	4.71
A6			8.02		7.93		6.34	2.57	2.31	4.67	4.01

Mithramycin Di- and Trisaccharide Protons							
sugar	H1	H2a	H2e	H3/CH_3	H4	H5	CH_3-5
A	5.32	2.03	2.84	4.08	3.26	3.68	1.43
B	5.15	1.63	2.16	3.65	3.04	3.65	1.32
C	4.66	1.85	2.30	1.97	2.96	2.85	1.29
D	2.45	1.18	2.31	3.61	3.68	3.46	1.19
E	5.22	1.65	2.22	1.39[c]	3.04	3.83	1.45

Mithramycin Aglycon Protons												
aglycon	H2	H4a,4e	H3	H5	H10	CH_3-7	H1′	OCH_3	H3′	H4′	CH_3-4′	HO8
Mth	4.38	2.60, 2.74	2.74	6.83	6.57	2.52	4.95	3.40	4.21	4.28	1.29	16.1

[a] Buffer solution contains 0.1 M NaCl, 10 mM phosphate, and 1 mM EDTA. The nonexchangeable proton data were obtained in D_2O, pH 6.5, at 25 °C; the exchangeable proton data were obtained in H_2O, pH 6.5, at 15 °C. [b] Chemical shift at pH 6.5 and 5 °C. [c] CH_3 chemical shift.

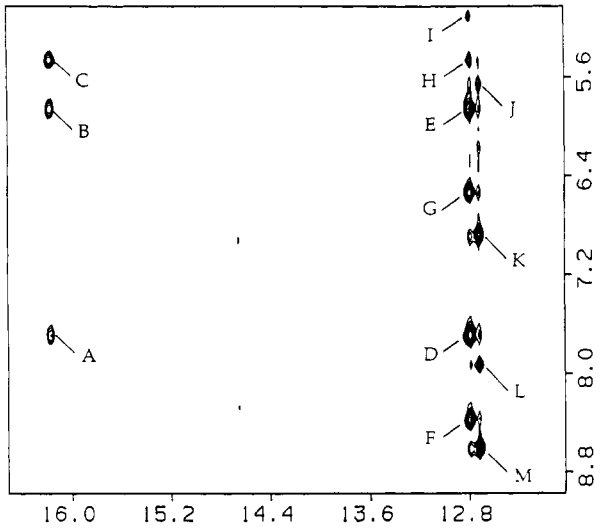

FIGURE 2: Expanded NOESY (170-ms mixing time) contour plot correlating the 16.4–12.0 ppm region with the 8.8–5.2 ppm region in the Mg^{2+}-coordinated Mth dimer–d(T-C-G-C-G-A) complex in D_2O buffer at 18 °C. Cross peaks A–G are assigned as follows: A, Mth(OH8)–G3(NH_2,b); B, Mth(OH8)–G3(NH_2,e); C, Mth(OH8)–C4(H1′); D, G3(NH1)–G3(NH_2b); E, G3(NH1)–G3(NH_2,e); F, G3(NH1)–C4(NH_2-4,b); G, G3(NH1)–C4 (NH_2-4,e); H, G3-(NH1)–C4(H1′); I, G3(NH1)–C4(H5); J, G5(NH1)–C2(H5); K, G5(NH1)–C2(NH_2-4,e); L, G5(NH1)–A6(H2); M, G5(NH)–C2-(NH_2-4,b).

single phenolic hydroxyl resonance is detected at 16.1 ppm and is assigned to the C^8 hydroxyl on the aglycon chromophore on the basis of an NOE to adjacent C^7 methyl protons. Two narrow resonances are partially resolved at 12.75 and 12.80 ppm and must originate in the nonterminal guanine imino protons in the complex.

The exchangeable protons have been assigned following analysis of the NOESY spectrum (170-ms mixing time) of the Mg^{2+}-coordinated Mth dimer–d(T-C-G-C-G-A) complex in H_2O buffer at 18 °C. An expanded plot establishing NOE connectivities between the 12.0–16.4 ppm phenolic and imino protons and the 5.2–8.8 ppm base and amino proton regions is plotted in Figure 2. The G3 imino proton at 12.80 ppm exhibits NOEs to its own amino protons (peaks D and E, Figure 2) and the amino protons of C4 (peaks F and G, Figure 2). This result demonstrates slow rotation about the guanine C^2–NH_2 bond for the Wastson–Crick G3·C4 base pairs in the complex (Patel, 1976). The observed NOEs between the 12.75 ppm G5 imino proton and the amino protons of C2 (peaks M and K, Figure 2) establish formation of Watson–Crick C2·G5 base pairs in the complex. The exchangeable proton assignments in the complex are listed in Table I.

We observe a set of intermolecular NOEs between the C^8 hydroxyl proton of the aglycon and the amino protons of G3 (peaks A and B, Figure 2) and the H1′ proton of C4 (peak C, Figure 2) in the complex. These intermolecular NOEs establish that the mithramycin dimer binds in the minor groove of the duplex and that the C^8-containing edge of the aglycon chromophores is positioned opposite the (G3-C4)·(G3-C4) step in the complex.

Nucleic Acid Nonexchangeable Proton Assignments in the Complex. The proton spectrum of the Mg^{2+}-coordinated Mth dimer–d(T-C-G-C-G-A) complex in D_2O buffer, pH 6.5 at 25 °C, is plotted in Figure 1B. The nonexchangeable protons are well resolved and have been assigned following analysis of two-dimensional NOESY, DQF-COSY, HOHAHA, and RELAY-COSY data sets of the complex in D_2O buffer at 25 °C. An expanded NOESY (250-ms mixing time) contour plot of the complex establishing NOE connectivities between the 7.0–8.2 ppm base protons and the 5.0–6.4 ppm sugar H1′ protons is plotted in Figure 3A. We can trace connectivities between base protons (purine H8 and pyrimidine H6) and their own and 5′-flanking sugar H1′ protons from the 5′ to the 3′ end of the d(T1-C2-G3-C4-G5-A6) sequence in the complex (Hare et al., 1983). An expanded NOESY (250-ms mixing time) contour plot of the complex establishing NOE connectivities between the 7.0–8.2 ppm base protons and the 1.2–3.2 ppm sugar H2′ and 2″ protons is plotted in Figure 3B. The same pattern of NOEs between base protons and their own and 5′-flanking sugar H2′ and H2″ protons is detected in the contour plot with the chain tracing involving the sugar H2′ protons plotted in Figure 3B. We note that the NOEs between the H6 proton of C4 and its own H2′ and H2″ protons are unusually weak, indicative of a change in sugar pucker at C4 in the complex. The nonexchangeable proton assignments in the complex are listed in Table I.

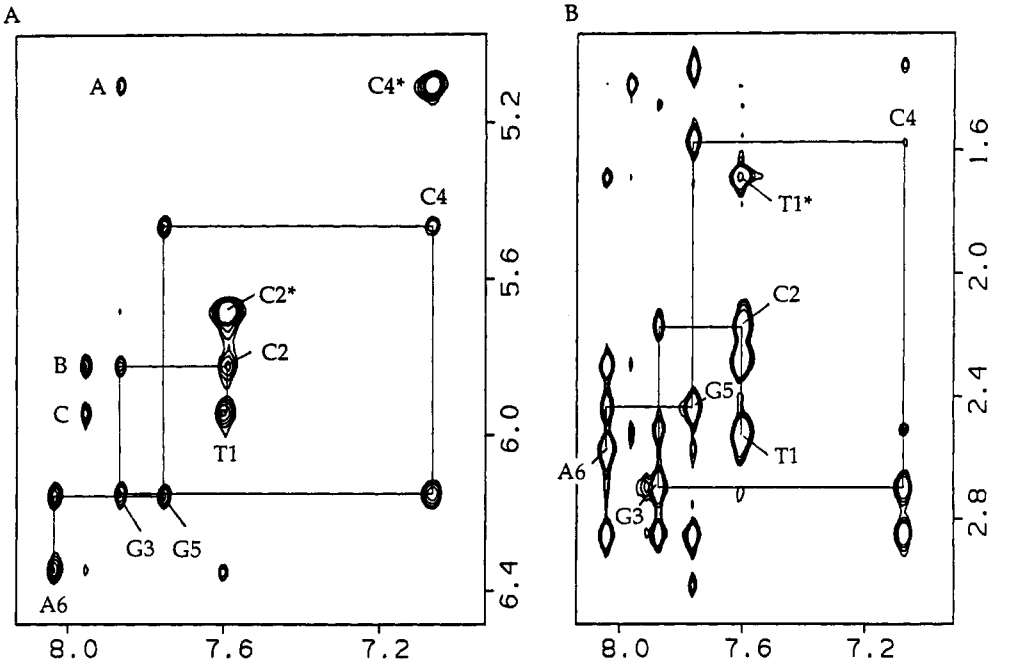

FIGURE 3: Expanded NOESY (250-ms mixing time) contour plots in the Mg^{2+}-coordinated Mth dimer–d(T-C-G-C-G-A) complex in D_2O buffer, pH 6.5 at 25 °C. (A) Expanded plot establishing distance connectivities between the base (7.0–8.2 ppm) and the sugar H1′ and cytidine H5 protons (5.0–6.4 ppm). The lines trace the NOE connectivities between base protons and their own and 5′-flanking sugar H1′ protons. Cytidine H5–H6 cross peaks are designated by asterisks. Cross peaks A–C are assigned as follows: A, G3(H8)–C4(H5); B, A6(H2)–C2(H1′); C, A6(H2)–T1(H1′). (B) Expanded plot establishing distance connectivities between the base (7.0–8.2 ppm) and the sugar H2′ and 2″ protons (1.2–3.2 ppm). The lines trace the connectivities between base protons and their own and 5′-flanking sugar H2′ protons. The thymine H6–CH_3 cross peak is designated by an asterisk.

Nucleic Acid Complexation Shifts. The exchangeable and nonexchangeable nucleic acid proton chemical shift changes on proceeding from the d(T-C-G-C-G-A) duplex to the Mg^{2+}-coordinated Mth dimer–d(T-C-G-C-G-A) complex are listed in Table SI (supplementary material). The largest chemical shift changes are detected at the C4 and G5 residues and include upfield shifts at the minor groove H2″ (0.83 ppm) and H4′ (2.80 ppm) protons of C4 and downfield shifts at the minor groove H1′ (–0.45 ppm) and H4′ (–0.76 ppm) protons of G5 on proceeding from the duplex to the complex.

Mithramycin Nonexchangeable Proton Assignments in the Complex. The nonexchangeable mithramycin protons in the Mg^{2+}-coordinated Mth dimer–d(T-C-G-C-G-A) complex in D_2O buffer at 25 °C have been assigned following analysis of NOESY, DQF-COSY, HOHAHA, and RELAY-COSY data sets. Expanded contour plots of the symmetrical 1.0–5.4 ppm region of the complex in D_2O buffer at 25 °C are plotted in Figure 4, with the cross peaks above the diagonal originating in a NOESY (250-ms mixing time) data set and the corresponding cross peaks below the diagonal originating in a DQF-COSY data set. The distance connectivities in the NOESY contour plot and the coupling connectivities in the DQF-COSY contour plot for the A sugar ring of the mithramycin dimer in the complex are traced in Figure 4. In addition, the A sugar can be linked to the B sugar on the basis of interresidue NOEs detected between the A(H3) and B(H1) proton pairs (peak A, Figure 4) and between the A(H1) and B(H1) proton pairs (peak B, Figure 4) in the complex. The same procedure was used to approach the B-sugar protons and the sugar protons in the C-D-E trisaccharide segment in the complex. The aglycon, side-chain, and sugar protons of the mithramycin dimer in the complex are tabulated in Table I.

Mithramycin Complexation Shifts. Several drug protons exhibit unusual chemical shifts in the Mg^{2+}-coordinated Mth dimer–d(T-C-G-C-G-A) complex (Table I). These include

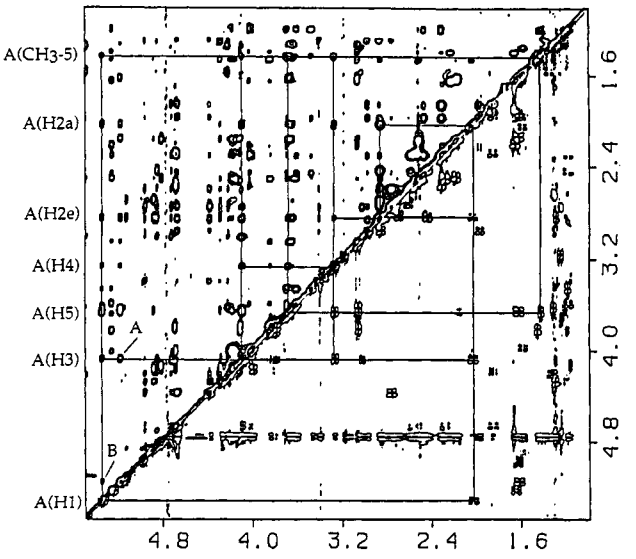

FIGURE 4: Composite plot of the NOESY (250-ms mixing time) contour plot (above the diagonal) and the DQF-COSY contour plot (below the diagonal) for the expanded symmetrical 5.4–1.0 ppm region of the Mg^{2+}-coordinated Mth dimer–d(T-C-G-C-G-A) complex in D_2O buffer, pH 6.5 at 25 °C. The lines trace the NOESY distance and DQF-COSY coupling connectivities among protons in the A-sugar ring. Cross peaks A and B correspond to NOEs between A- and B-sugar protons. These are assigned as follows: A, B(H1)–A(H3); B, B(H1)–A(H1).

large upfield shifts at the H3 proton of the C sugar and the H1 proton of the D sugar and smaller upfield shifts at the H1 and H5 protons of the C sugar.

Nucleic Acid Proton Coupling Patterns in the Complex. The vicinal proton sugar coupling constant patterns in the Mg^{2+}-coordinated Mth dimer–d(T-C-G-C-G-A) complex in D_2O buffer at 25 °C have been monitored in two-dimensional correlation experiments. An expanded contour plot correlating vicinal couplings between sugar H1′ and sugar H2′ and H2″

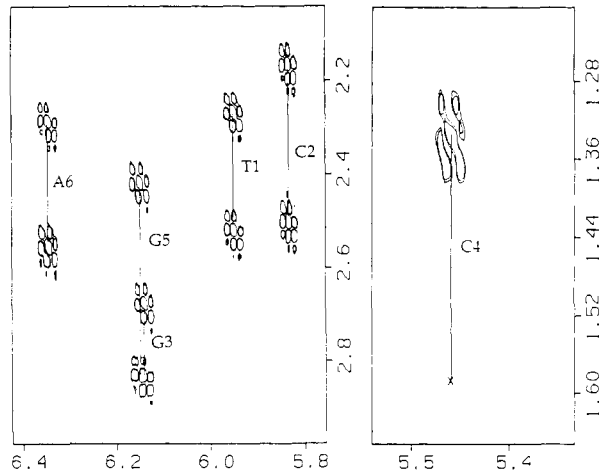

FIGURE 5: Expanded phase-sensitive COSY-45 contour plot of the Mg^{2+}-coordinated Mth dimer–d(T-C-G-C-G-A) complex in D_2O buffer, pH 6.5 at 25 °C, showing coupling connectivities between sugar H1′ and sugar H2′ and H2″ protons. The coupling cross peak between the sugar H1′ and H2′ protons of C4 is absent (designated by ×) in the complex.

protons in a COSY-45 experiment is plotted in Figure 5. We detect coupling cross peaks for H1′–H2′ and H1′–H2″ proton pairs for the T1, C2, G3, G5, and A6 sugars in the complex. By contrast, the H1′–H2′ cross peak is absent for the C4 sugar in the complex (Figure 5), indicative of a change in sugar pucker at this residue on complex formation.

Mithramycin Coupling Patterns in the Complex. We observe similar coupling constant patterns in two-dimensional correlation contour plots for mithramycin in D_2O buffer, pH 6.0 at 25 °C, and for the Mg^{2+}-coordinated Mth dimer–d(T-C-G-C-G-A) complex in D_2O buffer, pH 6.5 at 25 °C. Our coupling data establishes that OH-4 adopts an axial position and that CH_3-5 adopts an equitorial position for the D sugar, and this result requires reversal of the chirality at the C^4 carbon (Altona & Haasnoot, 1980) of the D sugar from what had been reported previously (Thiem & Meyer, 1981). Thus, we observe a weak coupling cross peak between D(H3) and D(H4), while no coupling cross peak is observed between D(H4) and D(H5) in both the free drug and the complex. Similarly, our NMR data require a reversal of chirality at the C^4 carbon of the A sugar from previously reported results (Thiem & Meyer, 1981). The H2 and H3 protons in the aglycon exhibit a strong cross peak consistent with their axial orientations, thus positioning the bulky hydrophilic side chain and the C-D-E trisaccharide groups in equatorial orientations.

Head-to-Tail Alignment of the Mithramycin Dimer in the Complex. Previous NMR studies in solution (Gao & Patel, 1989a; Gao et al., 1992) and in the crystalline state (C. Ogata, X. Gao, and W. Hendrickson, personal communication) established that the Mg^{2+}-coordinated chromomycin dimer bound in a head-to-tail alignment to the d($T_2G_2C_2A_2$) duplex. We observe a set of NOEs between mithramycin protons that support a similar head-to-tail alignment of the Mg^{2+}-coordinated mithramycin dimer to the d(T-C-G-C-G-A) duplex. Several of these NOEs (peaks C–L, Figure 6) are assigned in the expanded NOESY contour plot outlining distance connectivities between the 4.8–8.0 ppm and the 1.0–4.4 ppm regions of the complex. Thus, NOEs are detected between the aglycon H5 proton and the H1 and H2a (or CH_3-5) protons of the D sugar (peaks D and E, Figure 6) and between the aglycon H10 proton and the H1, H2a (or CH_3-5), and H5 protons of the D sugar (peaks G, J, and K, Figure 6). In addition NOEs are detected between the aglycon CH_3-7

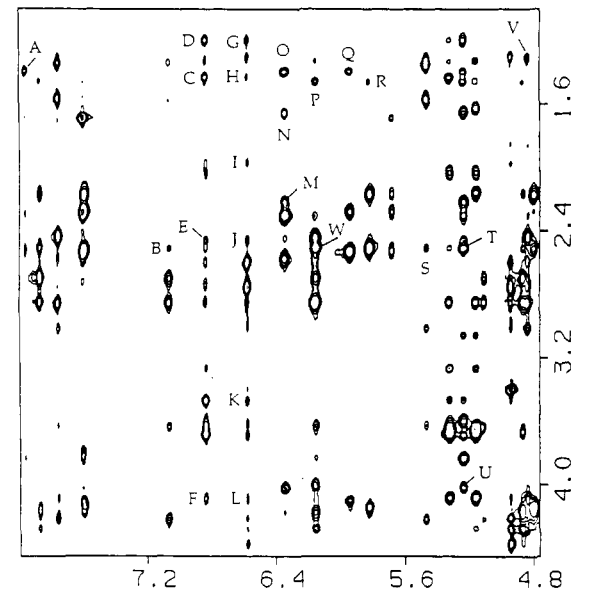

FIGURE 6: Expanded NOESY (250-ms mixing time) contour plot of the Mg^{2+}-coordinated Mth dimer–d(T-C-G-C-G-A) complex in D_2O buffer, pH 6.5 at 25 °C. The cross peaks establish distance connectivities between the 4.8–8.0 ppm and the 1.0–4.4 ppm region. Cross peaks A–W are assigned as follows: A, A6(H2)–E(CH_3-3); B, C4(H6)–Mth(CH_3-7); C, Mth(H5)–A(CH_3-5); D, Mth(H5)–D(H2a,CH_3-5); E, Mth(H5)–D(H1); F, Mth(H5)–A(H3); G, Mth(H10)–D(H2a,CH_3-5); H, Mth(H10)–A(CH_3-5); I, Mth(H10)–C(H3); J, Mth(H10)–D(H1); K, Mth(H10)–D(H5); L, Mth(H10)–A(H3); M, A6(H1′)–E(H2e); N, A6(H1′)–E(H2a); O, A6(H1′)–E(CH_3-3); P, G3(H1′)–E(CH_3-5); Q, T1(H1′)–E(CH_3-3); R, C2(H1′)–E(CH_3-5); S, C4(H1′)–Mth(CH_3-7); T, E(H1)–Mth(CH_3-7); U, E(H1)–A6(H4′); V, G5(H3′)–Mth(CH_3-4′); W, G3(H1′)–Mth(CH_3-7).

and E-sugar H5 protons, as well as between the A-sugar and D-E-sugar protons, consistent with a head-to-tail alignment of the Mg^{2+}-coordinated mithramycin dimer in the complex.

Intermolecular NOEs in the Complex. We have detected a large set of intermolecular NOEs between the Mg^{2+}-coordinated mithramycin dimer and the d(T-C-G-C-G-A) duplex which define the intermolecular contacts stabilizing the complex. Several of these intermolecular NOEs are assigned in the expanded NOESY contour plot in Figure 6 (peaks A, B, and M–W), and a complete listing is tabulated in Table II. The mithramycin dimer must bind to the minor groove since the intermolecular NOEs from the drug are to the DNA minor groove guanine NH_2-2, adenine H2, and sugar H1′, H2″, and H4′ protons in the complex (Table II).

The aglycon protons (CH_3-7, OH-8, and H10) exhibit intermolecular NOEs to the minor groove protons of G3, C4, and G5 (Table II), which requires that the aglycons of the mithramycin dimer are positioned opposite the central (G3-C4-G5)·(G3-C4-G5) segment of the duplex in the complex. The C-sugar protons (H2a and H3) are positioned opposite the H4′ proton of G5, while the D-sugar protons (H1, H2e, H3, and H4) are positioned opposite the H4′ proton of A6 in the complex (Table II). There are also extensive intermolecular contacts between the E-sugar protons (H1, H2a,e, CH_3-3, and H5) and the minor groove protons of A6 (H2, H1′, and H4′) in the complex (Table II). These intermolecular NOEs are consistent with the C-D-E trisaccharide segments of the mithramycin dimer being positioned in the minor groove and directed toward the 3′-end of the duplex in the complex.

Phosphorus Assignments in the Complex. We detect five resolved phosphorus resonances in the proton decoupled phosphorus spectrum of the Mg^{2+}-coordinated Mth dimer–d(T-C-G-C-G-A) complex in D_2O buffer at 25 °C (Figure

Table II: Intermolecular NOEs between Mithramycin and DNA Oligomer Protons in the Mg^{2+}-Coordinated Mth Dimer–d(T-C-G-C-G-A) Complex

mithramycin protons	DNA protons
chromophore	
Mth(HO8)	G3(NH_2b,e), G3(NH), C4(H1′)
Mth(H10)	G5(H4′)
Mth(CH_3-7)	G3(H1′), G3(H4′), C4(H1′), C4(H6)
Mth(H1′)	G5(H4′), G5(H2″)
Mth(CH_3-4′)	G5(H3′)
A sugar	
A(H2a)	G3(H4′)
B sugar	
B(H1)	G3(H4′), G3(H3′)
B(H2e)	G3(H3′)
C sugar	
C(H2a)	G5(H4′)
C(H3)	G5(H4′)
D sugar	
D(H1)	A6(H4′)
D(H2e)	A6(H4′)
D(H3)	A6(H4′)
D(H4)	A6(H4′)
E sugar	
E(H1)	A6(H4′)
E(H2a, H2e)	A6(H1′), A6(H4′)
E(CH_3-3)	A6(H2), A6(H1′), T1(H1′)
E(H5)	A6(H1′), A6(H4′)
E(CH_3-5)	G3(H1′), C2(H1′), G3(H4′)

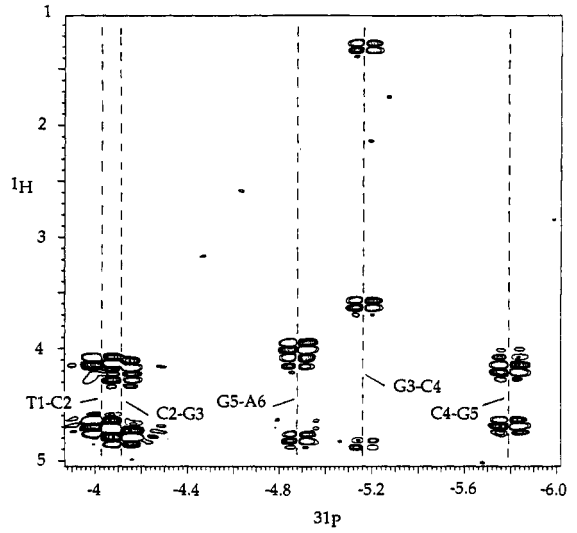

FIGURE 7: Expanded contour plot of the proton-detected proton–phosphorus correlation experiment with the Mg^{2+}-coordinated Mth dimer–d(T-C-G-C-G-A) complex in D_2O buffer at 27 °C. We detect coupling connectivities between individual phosphates and their 5′-linked H3′ protons and their 3′-linked H5′, H5″, and H4′ protons. The assignments of the phosphorus resonances follow from the known sugar proton assignments.

1C). These phosphorus resonance assignments are based on coupling correlations to their assigned 3′-linked H4′ protons and their 5′-linked H3′ protons in the complex. These couplings connectivities are readily made in the expanded proton-detected phosphorus-proton correlation contour plot of the complex in D_2O buffer at 27 °C (Figure 7), and the phosphorus assignments are listed both in Figure 7 and in Table III. Thus, the G5-A6 (–4.88 ppm), G3-C4 (–5.16 ppm), and C4-G5 (–5.80 ppm) phosphates in the complex (Figure 7) are shifted out of the –4.0 to –4.5 ppm spectral range characteristic of unperturbed phosphates.

Carbon Assignments. Carbon chemical shifts are dispersed over a larger chemical shift range than are proton shifts, and hence carbon chemical shift classification by sugar carbon type can be readily distinguished even in the presence of ring current contributions. This point is important in the Mg^{2+}-coordinated Mth dimer–d(T-C-G-C-G-A) complex, where several protons are dramatically shifted out of their normal ranges by ring current contributions (Table I). The carbon chemical shifts were assigned from one-bond carbon–proton couplings in a proton-detected carbon–proton correlation experiment on the Mg^{2+}-coordinated Mth dimer–d(T-C-G-C-G-A) complex in D_2O buffer at 25 °C. These carbon assignments are listed in Table SII (supplementary material) and are based on correlation to the assigned attached protons in the complex. We were unable to unambiguously assign the methylene carbons of both the drug sugars and the DNA sugars in the complex.

Table III: Proton–Phosphorus Correlations and Phosphorus Resonance Assignments (ppm) in the Mg^{2+}-Coordinated Mth Dimer–d(T-C-G-C-G-A) and Mth Dimer–d(T-G-G-C-C-A) Complexes in D_2O Buffer

dinucleotide step	^{31}P	5′-H3′	3′-H4′
	d(T-C-G-C-G-A) complex		
T1-C2	–4.03	4.67	4.12
C2-G3	–4.11	4.76	4.26
G3-C4	–5.16	4.86	1.31
C4-G5	–5.80	4.20	4.68
G5-A6	–4.86	4.82	4.00
	d(T-G-G-C-C-A) complex		
T1-G2	–4.00	4.69	4.41
G2-G3	–4.13	4.99	4.29
G3-C4	–4.84	4.67	1.52
C4-C5	–5.64	4.18	4.48
C5-A6	–4.69	4.76	4.08

Mth Dimer–d(T-G-G-C-C-A) Complex. We have undertaken a parallel NMR characterization of the Mg^{2+}-coordinated Mth dimer–d(T-G-G-C-C-A) complex which contains a central (G-G-C-C) segment in contrast to the central (C-G-C-G) segment for the complex presented in the previous section. The exchangeable and nonexchangeable proton spectra of the d(T-G-G-C-C-A) complex in aqueous buffer are presented in Figure S1 (supplementary material). The spectra exhibit excellent resolution, with the complex retaining 2-fold symmetry. An expanded NOESY (250-ms mixing time) contour plot of the d(T-G-G-C-C-A) complex establishes that the base-to-sugar H1′ distance connectivities can be traced without interruption along the entire hexanucleotide sequence in the complex (Figure S2A, supplementary material). An expanded DQF-COSY contour plot of the d(T-G-G-C-C-A) complex establishes the presence of H1′–H2′ and H1′–H2″ coupling cross peaks for all residues, except that the H1′–H2′ cross peak for the C4 sugar is missing (Figure S2B, supplementary material). The complete proton assignments for the Mg^{2+}-coordinated Mth dimer–d(T-G-G-C-C-A) complex are listed in Table IV, and the assigned intermolecular NOEs are listed in Table V. The proton decoupled phosphorus spectrum of the d(T-G-G-C-C-A) complex is presented in Figure S3A (supplementary material). The phosphorus assignments for this complex are listed in Table III and are based on the correlated experiment outlined in Figure S3B.

The proton and phosphorus chemical shift values, the intramolecular and intermolecular NOE patterns, and the proton–proton coupling patterns are very similar for the Mg^{2+}-coordinated Mth dimer complexes with the d(T-C-G-C-G-A) and d(T-G-G-C-C-A) self-complementary duplexes. We have therefore focused our efforts below on the structure determination of one representative member of this family, namely, the Mg^{2+}-coordinated Mth dimer–d(T-C-G-C-G-A) complex.

Table IV: Proton Chemical Shifts in the Mg^{2+}-Coordinated Mth Dimer–d(T-G-G-C-C-A) Complex[a]

d(T-G-G-C-C-A) Protons

residue	NH	NH_2b,e	H8	H6	H2	H5/CH_3	H1′	H2′	H2″	H3′	H4′	H5′,5″
T1				7.49		1.68	5.95	2.04	2.45	4.69	4.09	3.75
G2	12.99		7.93				6.11	2.79	2.91	4.99	4.41	4.14
G3	12.88	7.94, 6.06	7.39				6.04	2.68	2.68	4.65	4.30	4.22, 4.49
C4		8.22, 6.63		7.23		5.17	5.68	2.02	1.58	4.18	1.51	3.58
C5		8.57, 6.80		7.56		5.48	6.31	2.00	2.42	4.78	4.48	4.14, 3.27
A6			8.28		7.77		6.38	2.66	2.43	4.70	4.08	

Mithramycin Di- and Trisaccharide Protons

sugar	H1	H2a	H2e	H3/CH_3	H4	H5	CH_3-5
A	5.37	2.11	2.88	4.15	3.31	3.70	1.44
B	5.09	1.65	2.27	3.70	3.08	3.70	1.33
C	4.67	1.78	2.29	2.06	2.96	2.90	1.30
D	2.57	1.33	1.77	3.66	3.78	3.49	1.22
E	5.29	1.75	2.18	1.47[b]	3.17	3.99	1.49

Mithramycin Aglycon Protons

aglycon	H2	H4a,4e	H3	H5	H10	CH_3-7	H1′	OCH_3	H3′	H4′	CH_3-4′	HO8
Mth	4.38	2.60, 2.74	2.74	6.83	6.57	2.52	4.95	3.40	4.21	4.28	1.29	16.1

[a] Buffer solution contains 0.1 M NaCl, 10 mM phosphate, and 1 mM EDTA. The nonexchangeable proton data were obtained in D_2O, pH 7.0, at 18 °C; the exchangeable proton data were obtained in H_2O, pH 7.0, at 18 °C. [b] CH_3 chemical shift.

Table V: Intermolecular NOEs between Mithramycin and DNA Oligomer Protons in the Mg^{2+}-Coordinated Mth Dimer–d(T-G-G-C-C-A) Complex

mithramycin protons	DNA protons
chromophore	
Mth(HO8)	G3(NH_2b,e), G3(NH)
Mth(HO8)	C4(H1′)
Mth(H10)	C5(H4′)
Mth(CH_3-7)	C4(H1′), G3(H2′, H2″)
Mth(CH_3-7)	G3(H1′), G3(H4′)
A sugar	
A(H2e)	G3(H4′)
A(H2a)	G3(H4′)
B sugar	
B(H3), B(H5)	G3(H4′)
B(H1)	G3(H4′)
C sugar	
C(H2a)	C5(H1′)
C(H2a), C(H2e)	C5(H4′)
D sugar	
D(H2a)	A6(H4′)
D(H2e)	A6(H4′)
E sugar	
E(H2e)	A6(H1′), A6(H4′)
E(CH_3-3)	A6(H2), A6(H1′)
E(H5)	G3(H1′), G3(H4′)
E(CH_3-5)	G3(H1′), G2(H1′), G3(H4′)

Restrained Molecular Dynamics and Relaxation Matrix Refinement. Two different starting structures, referred to as Init-A and Init-B, were generated for structure calculations. The Init-A structure was obtained by docking the mithramycin dimer onto the minor groove of a standard A-form d(T-C-G-C-G-A) duplex. The Init-B structure was obtained by docking the mithramycin dimer on a standard B-form d(T-C-G-C-G-A) duplex. These Init-A and Init-B starting structures are drawn in Figure S4 (suppelementary material). Due to the narrow minor groove in B-form duplexes, there were a number of unfavorable van der Waals contacts in the Init-B starting structure. These relatively bad contacts were relieved by conjugate gradient energy minimization, during which a purely repulsive potential was maintained to give the energy-minimized EM-A and EM-B structures. The two starting structures differ in the conformation of the duplex and the orientation of the chromophores of mithramycin in the dimer. The root mean square deviation between all atoms in Init-A and Init-B was 3.20 Å and increased to 4.0 Å between EM-A and EM-B structures.

Table VI: Relaxation Matrix Refinement and Molecular Dynamics Protocol

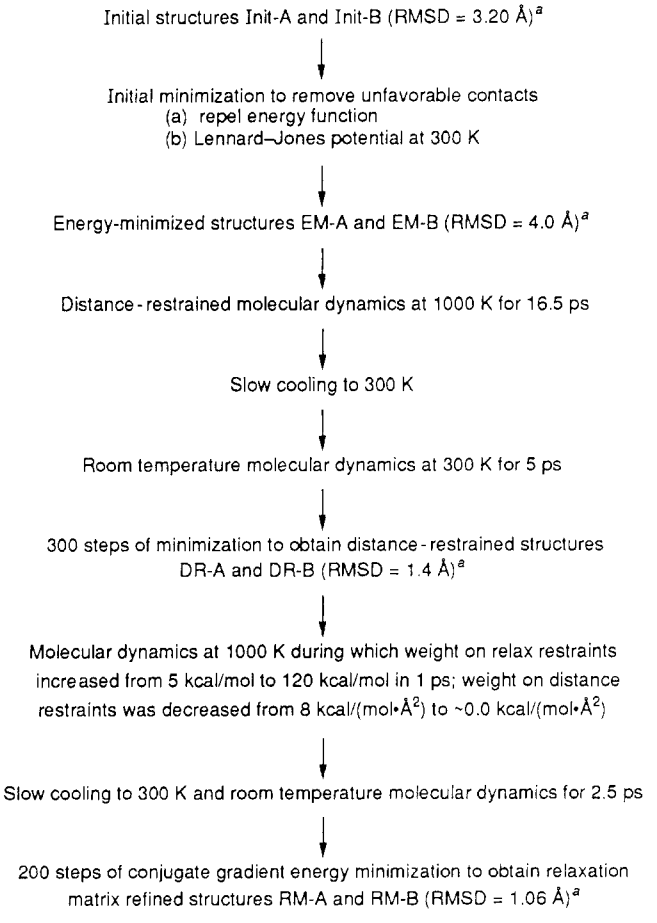

[a] RMSD, root mean square deviation.

Each of the energy-minimized structures was subjected to distance-restrained molecular dynamics followed by relaxation matrix refinement as discussed in the Materials and Methods section. The refinement protocol is summarized in Table VI.

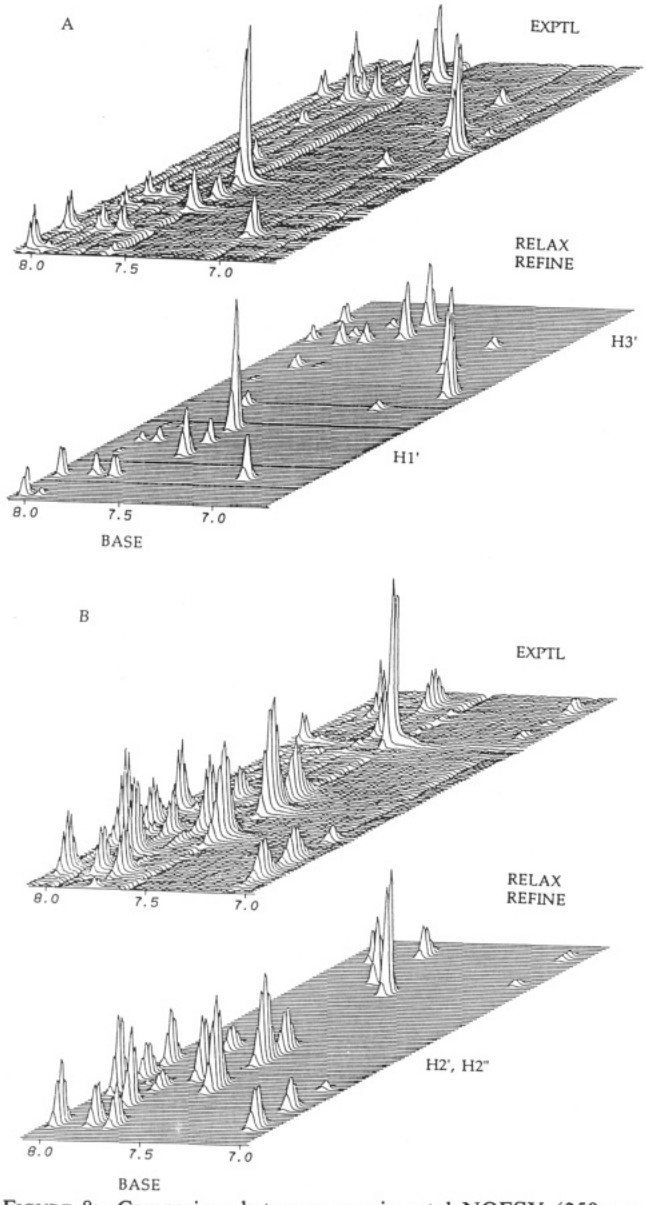

FIGURE 8: Comparison between experimental NOESY (250-ms mixing time) stacked plots of the Mg^{2+}-coordinated Mth dimer–d(T-C-G-C-G-A) complex in D_2O buffer at 25 °C (top) and corresponding calculated spectra for the relaxation matrix refined RM-B structure (bottom). Panel A compares expanded regions correlating the base protons with the sugar H1′ and H3′ protons. Panel B compares expanded regions correlating the base protons with the sugar H2′ and H2″ protons.

The root mean square deviation between the resulting DR-A and DR-B structures after distance-restrained molecular dynamics was 1.44 Å. It was found to be essential to include a high-temperature step during the subsequent relaxation matrix refinement to get a better fit of the calculated with the experimental NOESY spectra. During relaxation matrix refinement we used an overall correlation time of 4 ns, which was determined by performing a grid search to obtain a minimum value for the *R* factor. The root mean square deviation between all atoms between the RM-A and RM-B structures after relaxation matrix refinement was 1.06 Å. During the time course of refinement the *R* factor changed from 38% and 33% for the DR-A and DR-B distance refined structures to 14% and 13% for the RM-A and RM-B relaxation matrix refined structures, respectively.

The experimental NOESY (250-ms mixing time) stacked plots for the Mg^{2+}-coordinated Mth dimer–d(T-C-G-C-G-A) complex in D_2O buffer at 25 °C can be compared with their calculated relaxation matrix refined counterpart corresponding to structure RM-B to asses the goodness of fit. We have prepared such expanded stacked plots correlating the base protons with the sugar H1′ and H3′ protons (Figure 8A), correlating the sugar H2′ and H2″ protons (Figure 8B), and correlating the sugar H1′ protons with the sugar H2′ and H2″ protons (Figure S5, supplementary material). There is good agreement between experimental and calculated stacked plots with small discrepancies for cross peaks between the A6(H2) and the C2(H1′)/T1(H1′) proton pairs. These differences may originate in the significantly longer spin–lattice relaxation time for adenine H2 protons and the local mobility associated with terminal residues.

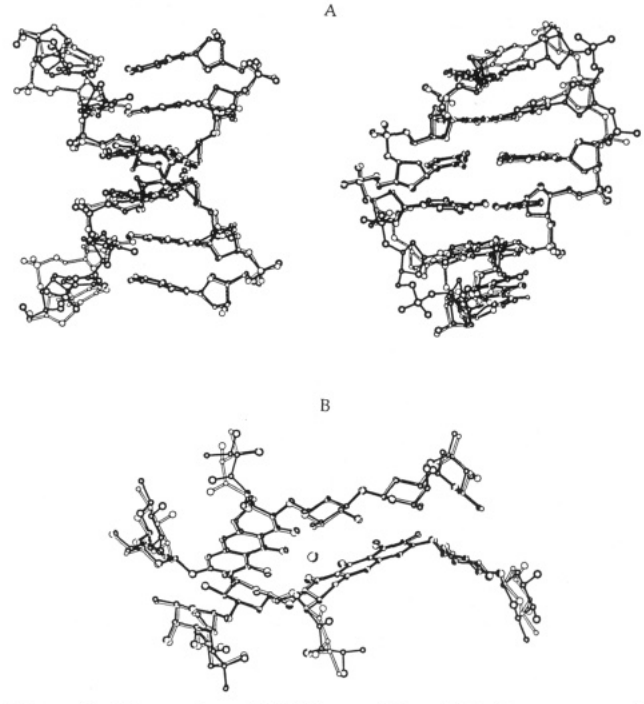

FIGURE 9: Comparison of (A) the nucleic acid duplex component and (B) the mithramycin dimer component in the superpositioned RM-A (open lines) and RM-B (closed lines) relaxation matrix refined structures of the Mg^{2+}-coordinated Mth dimer–d(T-C-G-C-G-A) complex.

The superpositioned relaxation matrix refined structures RM-A and RM-B of the complex are compared in Figure S6 (supplementary material). This comparison is difficult to visualize, and hence we have also compared the superpositioned DNA segments (Figure 9A) and the superpositioned mithramycin segments (Figure 9B) of the complex separately. We detect differences in the DNA component of the complex in the backbone at the T1-C2 segment between the RM-A and RM-B structures (Figure 9A). This most likely reflects the limited number of constraints involving the terminal T1 residue. There is good superposition of the mithramycin dimer segments between RM-A and RM-B refined structures (Figure 9B).

Structural Features of the Complex. Two different stereoviews of the relaxation matrix refined structure RM-B of the Mg^{2+}-coordinated Mth dimer–d(T-C-G-C-G-A) complex are shown in Figure 10. One view of the complex looks into the minor groove (Figure 10B), while the other is rotated by 90° along the helix axis (Figure 10A). The Mg^{2+}-coordinated mithramycin dimer–DNA complex exhibits 2-fold symmetry. The two chromophores are centered at the central G3-C4 step. Each mithramycin molecule spans one strand of the duplex DNA, such that the A-B disaccharide is oriented

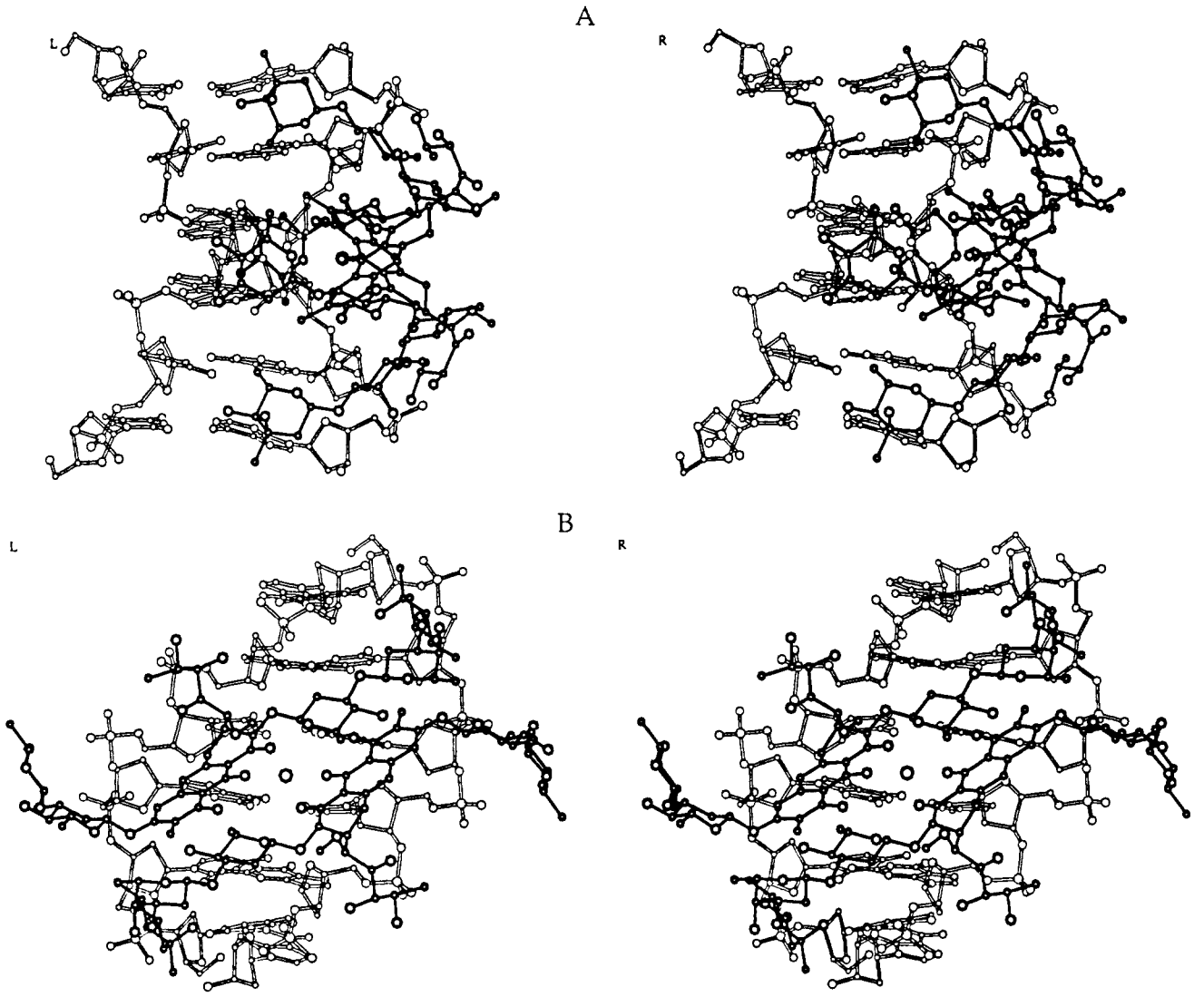

FIGURE 10: Stereopairs of the relaxation matrix refined RM-B structure of the Mg^{2+}-coordinated Mth dimer–d(T-C-G-C-G-A) complex. The DNA is shown by open lines, while the mithramycin dimer is shown by closed lines. The views in A and B are rotated by 90° along the helix axis. The view in B looks into the minor groove of the duplex.

Table VII: Twist and Rise Parameters between Adjacent Base Pairs for the d(T-C-G-C-G-A) Duplex[a] in the Relaxation Matrix Refined RM-B Structure of the Mg^{2+}-Coordinated Mth Dimer–d(T-C-G-C-G-A) Complex

step	twist	rise
T1-C2	35.7	2.57
C2-G3	22.7	2.88
G3-C4	37.4	4.34
C4-G5	22.7	2.89
G5-A6	35.7	2.57
B-DNA	36.0	3.38
A-DNA	32.7	2.56

[a] Obtained using the CURVES program (Lavery & Sklenar, 1988).

Table VIII: Individual Sugar Pseudorotation Values (P), Glycosidic Torsion Angles (χ), and X-Displacement Parameters for the d(T-C-G-C-G-A) Duplex[a] in the Relaxation Matrix Refined RM-B Structure of the Mg^{2+}-Coordinated Mth–d(T-C-G-C-G-A) Complex

residue	P	χ	base pair	X-disp[b]
T1	151.3	−108.9	T1·A6	−0.69
C2	42.3	−104.3	C2·G5	−0.91
G3	160.9	−107.6	G3·C4	−0.95
C4	18.0	−149.2		
G5	174.9	−104.2		
A6	141.0	−97.2		
B-DNA	162	−102		−0.71
A-DNA	18	−154		−5.43

[a] Obtained using the CURVES program (Lavery & Sklenar, 1988). [b] The X-displacement value is given for individual base pairs.

toward the 5′-end and the C-D-E trisaccharide is oriented toward the 3′-end of the duplex (Figure 10).

DNA Conformation in the Complex. We have evaluated the helical parameters for the DNA duplex in the relaxation matrix refined RM-B structure of the Mg^{2+}-coordinated Mth dimer–d(T-C-G-C-G-A) complex. The helical twist and rise parameters at individual steps are listed in Table VII, while the sugar pseudorotation values (P), the glycosidic torsion angles (χ) at individual residues, and the X-displacements of base pairs are listed in Table VIII. The corresponding helical parameters for the RM-A relaxation matrix refined structure are listed in Tables SIII and SIV (supplementary material). We detect systematic sequence-dependent perturbations in the helical parameters of the duplex in the complex compared to standard B-DNA and A-DNA helical values. We note that the helix exhibits an increased helical twist and rise at the central G3-C4 step, while it exhibits a decreased helical twist and rise at adjacent C2-G3 and C4-G5 steps in the RM-B refined structure (Table VII). The pseudorotation angles are characteristic of the C2′-*endo* family of sugar puckers for T1,

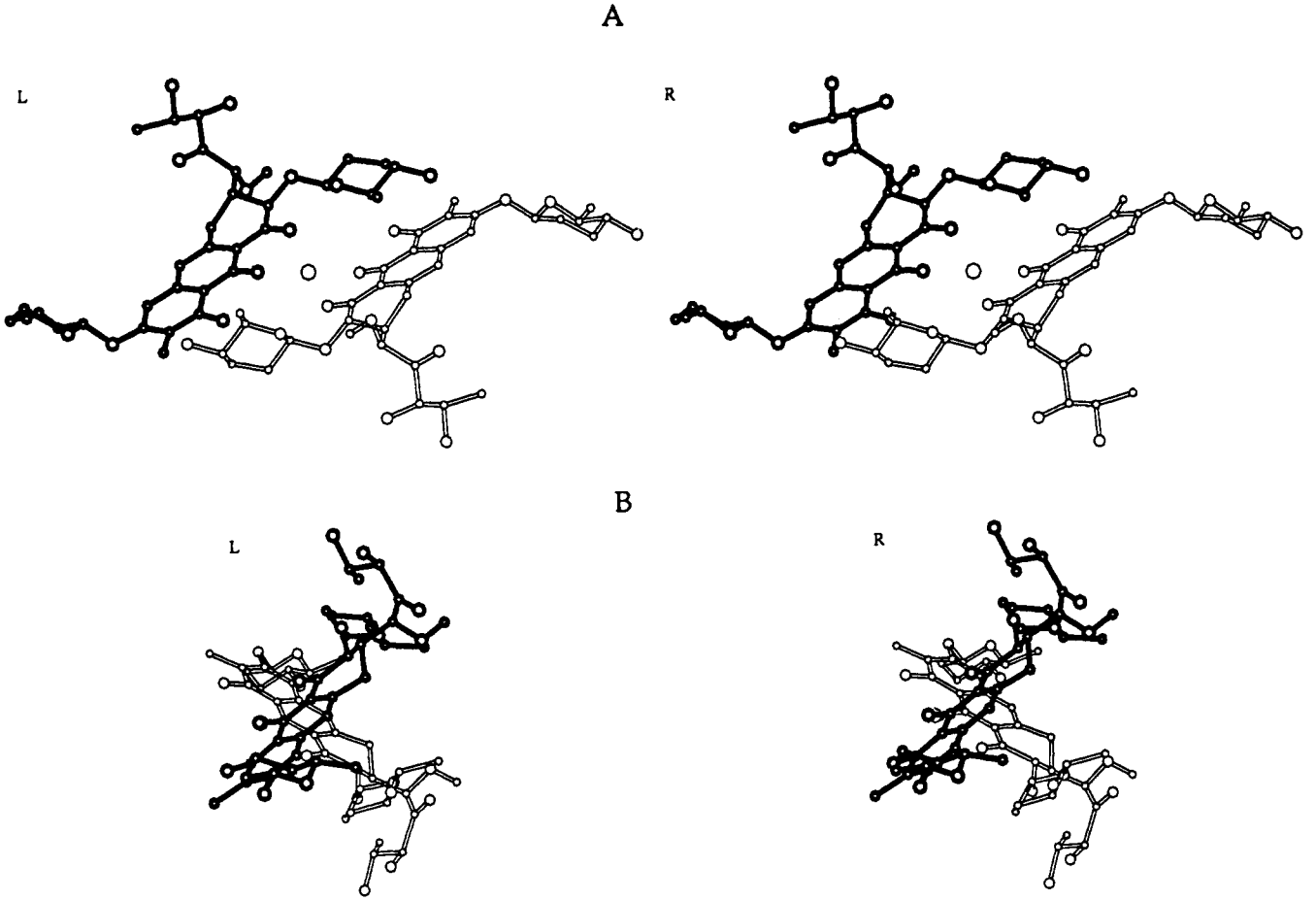

FIGURE 11: Stereopairs of two views of a truncated segment of the relaxation matrix refined RM-B structure of the Mg^{2+}-coordinated Mth dimer–d(T-C-G-C-G-A) complex. This segment emphasizes the coordination geometry at the Mg^{2+} divalent cation site. The aglycon and attached hydrophilic side chain along with the A and C sugars of one monomer are shown by open lines, while those of the other monomer are shown by closed lines. The Mg^{2+} cation is shown as a circle, and the divalent cation is coordinated to the O^9 enolate oxygens in an apical alignment and the O^1 carbonyl oxygens in adjacent in-plane orientations. Views A and B emphasize the mithramycin dimer orientation normal to the helix axis and differ by a 90° rotation along this axis.

G3, G5, and A6 and characteristic of the C3′-*endo* family of sugar puckers for C2 and C4 in the RM-B refined structure (Table VIII). The glycosidic torsion angles are in the B-DNA range for all residues except C4, which is in the A-DNA range in the RM-B refined structure (Table VIII). The X-displacements of the base pairs from the helix axis in the complex exhibit values in the B-DNA range (Table VIII). At the global level, the minor groove is both wide and shallow in the RM-B refined structure of the complex.

Mithramycin Dimer Conformation in the Complex. The drug dimer in the Mg^{2+}-coordinated Mth dimer–d(T-C-G-C-G-A) complex adopts a right-handed antiparallel alignment with all hexopyranoses in energetically favored chair conformations. The A-B disaccharide and the C-D-E trisaccharide units are in an extended conformation and span the entire minor groove of the hexanucleotide duplex in the complex. The torsion angles linking adjacent sugar residues of mithramycin in the RM-B refined structure are listed in Table IX.

The Mg^{2+}-coordinated aglycon planes are aligned with a slight tilt relative to each other with an angle of 53° between the two chromphore planes in the RM-B refined structure (Figure 11B). The Mg^{2+} cation coordinates the O^1 carbonyl oxygen and the O^9 phenolate anion oxygen of each aglycon in the RM-B refined structure (Figure 11A). The distances and angles defining this coordination in the Init-B starting and RM-B refined structures are listed in Table X. We detect

Table IX: Torsion Angles Linking Adjacent Sugar Residues in Mithramycin in the Relaxation Matrix Refined RM-B Structure of the Mg^{2+}-Coordinated Mth Dimer–d(T-C-G-C-G-A) Complex

glycosidic linkage	dihedral angle	angle (deg)
Mth–C sugar	C1–C2–C(O1)–C(C1)	−83.0
	C2–O1–C(C1)–C(C2)	159.4
C sugar–D sugar	C(C2)–C(C3)–D(O1)–D(C1)	−145.4
	C(C3)–D(O1)–D(C1)–D(C2)	155.0
D sugar–E sugar	D(C2)–D(C3)–E(O1)–E(C1)	−94.1
	D(C3)–E(O1)–E(C1)–E(C2)	156.6
Mth–A sugar	Mth(C5)–Mth(C6)–A(O1)–A(C1)	35.4
	Mth(C6)–A(O1)–A(C1)–A(C2)	137.4
A sugar–B sugar	A(C2)–A(C3)–B(O1)–B(C1)	−70.5
	A(C3)–B(O1)–B(C1)–B(C2)	131.8

significant changes in these values associated with the refinement process.

Intermolecular Interactions in the Complex. Examination of the relaxation matrix refined RM-B structure establishes that four sets of intermolecular interactions stabilize the complex formed by the Mg^{2+}-coordinated mithramycin dimer and its G·C-rich minor groove target site on the d(T-C-G-C-G-A) duplex. One set of interactions involves the Mg^{2+}-coordinated aglycons which are positioned opposite the central (G3-C4)·(G3-C4) minor groove segment of the duplex. Symmetry-related intermolecular hydrogen bonds between the C^9 hydroxyl oxygen acceptor on the aglycon and the G4 amino group hydrogen bond donor on the duplex (Table XI) account for the sequence specificity of the mithramycin dimer for G·C base pairs at (G-C)·(G-C) steps in the minor groove.

Table X: Distances and Angles at the Mg^{2+} Coordination Site in the Starting Init-B Structure and the Relaxation Matrix Refined RM-B Structure of the Mth Dimer–d(T-C-G-C-G-A) Complex

	initial (Init-B)	final (RM-B)
	Distances (Å)	
Mth(O1)–Mg	3.50, 3.75	2.38, 2.38
Mth(O9)–Mg	2.45, 3.17	2.05, 2.06
	Angles (deg)	
Mth(O1)–Mg–Mth(O9)[a]	51, 50	71.9, 72.0
Mth(O9)–Mg–Mth(O9)	86	178.0
Mth(O1)–Mg–Mth(O9)[b]	49, 44	109.3, 109.2
Mth(O1)–Mg–Mth(O1)[b]	52	84.2

[a] Intraresidue. [b] Interresidue.

Table XI: Hydrogen-Bonding Distances (between Heteroatoms) in the Relaxation Matrix Refined RM-B Structure of the Mg^{2+}-Coordinated Mth Dimer–d(T-C-G-C-G-A) Complex

	donor	acceptor	distance (Å)
sugar E–C2 base	E(C4-OH)	C2(O2)	3.3
sugar E–G5 base	E(C3-OH)	G5(N2)	3.0
sugar E–A6 base	E(C3-OH)	A6(N3)	2.7
Mth–G3 base	Alk-C4′(OH)	G5(OP)	3.2
Mth–G3 base	G3(NH_2e)	Mth(HO8)	2.9

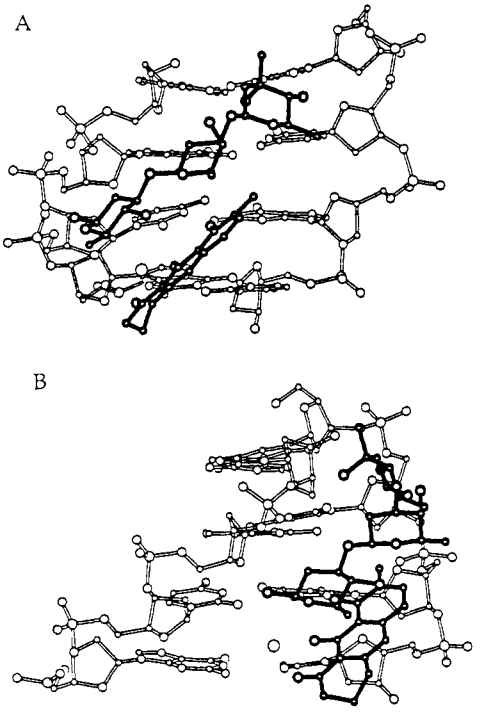

FIGURE 12: Truncated segment of the relaxation matrix refined RM-B structure of the Mg^{2+}-coordinated Mth dimer–d(T-C-G-C-G-A) complex. The aglycon ring of one monomer and the C-D-E trisaccharide segment of the other monomer are shown by closed lines. The (T1-C2-G3-C4)·(G3-C4-G5-A6) segment is shown by open lines. The views in A and B are rotated by 90° along the helix axis. The view in A emphasizes the stacking of the C-D disaccharide segment of one monomer on the aglycon chromophore of the other monomer. It also emphasizes that the C-D disaccharide interacts primarily with one strand of the duplex, while the E sugar is in the floor of the minor groove and interacts with both the strands of the duplex.

A second interaction involves the C-D disaccharide segment of one drug monomer and the aglycon of the second monomer which are aligned in parallel and together span the minor groove (C2-G3-C4)·(G3-C4-G5) segment on either side of the center of 2-fold symmetry of the complex (Figure 12). This alignment is stabilized by the stacking of the C-D disaccharide segment over the aglycon chromophore of its partner in the dimer such that the C and D sugars are directed edgeways toward the minor groove and primarily interact with one strand of the duplex. We also note that the other face of the same aglycon stacks over the sugar of C4 such that the aglycon is sandwiched between the C-D disaccharide segment and the sugar–phosphate backbone.

A third interaction involves the E-sugar residues which are positioned at either end of the mithramycin dimer and use one face of the sugar to interact with both strands at the (T1-C2)·(G5-A6) segment. The E sugar penetrates into the floor of the minor groove and forms a set of intermolecular hydrogen bonds involving donor hydroxyl hydrogens at the C3 and C4 positions on the E-sugar and acceptor atoms along the minor groove of the DNA (Table XI).

The fourth intermolecular interaction relates to the A-B disaccharide segment which is positioned opposite the sugar of G3 in the complex (Figure 13). The stereochemistry of the linkage between the A and B sugars of mithramycin (**2**) is such that the A-B disaccharide segment wraps around the minor groove edge of the sugar–phosphate backbone centered about the sugar of G3 in the complex.

We know little about the nature of the intermolecular interactions between the hydrophilic side chains of the mithramycin dimer and the minor groove edge of the DNA duplex due to the paucity of experimental constraints in this region of the complex. The hydrophilic side chain is positioned opposite the sugar–phosphate backbone centered about the C4-G5 step in the RM-B refined structure.

DISCUSSION

The present NMR study of the Mg^{2+}-coordinated Mth dimer–d(T-C-G-C-G-A) complex was greatly aided by the retention of the 2-fold symmetry of the self-complementary duplex on complex formation. The availability of high-resolution proton and phosphorus spectra of the complex and their two-dimensional homonuclear and heteronuclear counterparts has readily permitted analysis of through-space and through-bond connectivities to yield resonance assignments along with distance and pucker constraints.

Another NMR study has reported on the chemical shift and NOE parameters for a mithramycin–DNA oligomer complex (Banville et al., 1990b) using the assignment strategies reported earlier from our laboratory on chromomycin dimer–DNA oligomer complexes (Gao & Patel, 1989a). The current challenge is to go beyond spectral assignments and define the solution conformation of the mithramycin dimer–DNA complex by undertaking molecular dynamics calculations guided by the NMR-based distance constraints. This paper has defined the solution structure of the Mg^{2+}-coordinated Mth dimer–d(T-C-G-C-G-A) complex by iteratively minimizing differences between experimental and calculated NOESY spectra of the complex. The present contribution and an earlier solution structure of the Mg^{2+}-coordinated chromomycin dimer–d(A-A-G-G-C-C-T-T) complex (Gao et al., 1992) define how saccharide-containing antibiotics recognize and bind to the minor groove at G·C-rich sites on the duplex.

Sequence Specificity of Complex Formation. Our NMR studies have established that the same complex is formed when the Mg^{2+}-coordinated Mth dimer binds to the d(T-C-G-C-G-A) and d(T-G-G-C-C-A) self-complementary duplexes. Thus, both complexes exhibit very similar proton (Tables I and IV) and phosphorus (Table III) chemical shifts, intermolecular NOE patterns (Tables II and V), and DNA sugar

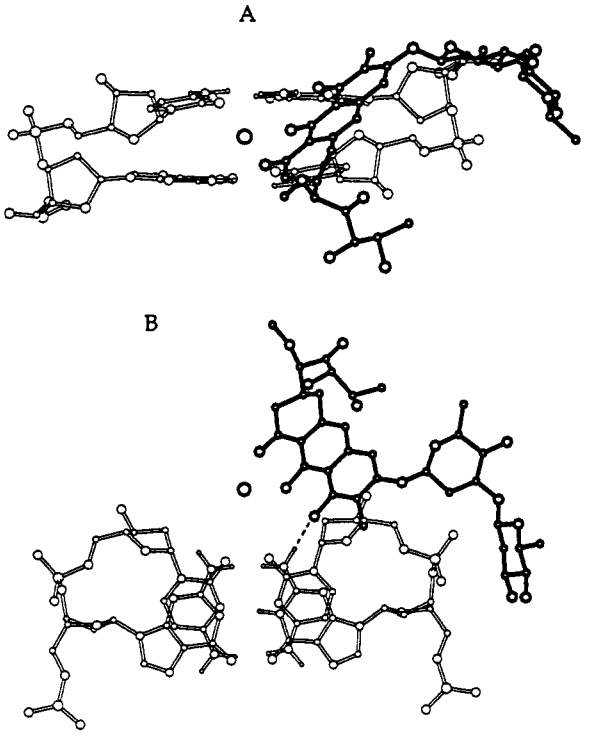

FIGURE 13: Truncated segment of the relaxation matrix refined RM-B structure of the Mg^{2+}-coordinated Mth dimer–d(T-C-G-C-G-A) complex. The aglycon with attached A-B disaccharide and hydrophilic side chain of one monomer in the mithramycin dimer is shown by closed lines. The (G3-C4)·(G3-C4) segment is shown by open lines. We have included the hydrogens from the NH_2-2 position of G3 in the drawings. View A is normal to the helix axis, while view B looks down the helix axis. The A-B disaccharide segment wraps around the minor groove edge of the sugar–phosphate backbone centered about the sugar of G3 in the complex in view B. This view shows the intermolecular hydrogen bond between the NH_2-2 group of G3 (donor) and the OH-9 of the aglycon (acceptor) which accounts for the sequence specificity of complex formation.

coupling constant patterns (Figures 5 and S2B). These results establish a strong binding site for the Mth dimer for the self-complementary d(T1-C2/G2-G3-C4-G5/C5-A6) duplex with little distinction between the C2·G5 and G2·C5 base pairs, which are one base pair removed in either direction from the center of symmetry of the complex. It appears at this time that the central G3-C4 step is essential for sequence-specific complex formation. The discussion below focuses on the relaxation matrix refined RM-B structure of the Mg^{2+}-coordinated Mth dimer–d(T-C-G-C-G-A) complex.

DNA Structure in the Complex. The NMR parameters establish that all base pairs adopt Watson–Crick alignment with *anti* glycosidic torsion angles for the DNA segment of the Mg^{2+}-coordinated Mth dimer–d(T-C-G-C-G-A) complex. Further, sequential base–sugar connectivities characteristic for antiparallel right-handed DNA duplexes can be traced along the entire d(T-C-G-C-G-A) chain in the complex (Figure 3).

The A and B families of antiparallel right-handed DNA helices can be differentiated on the basis of groove width dimensions, X-displacement of the bases relative to the helix axis, and sugar pucker/glycosidic torsion angle values. The observed minor groove width (defined as the shortest inter-strand phosphorus–phosphorus distance less 5.8 Å) of 8.6 Å in the refined RM-B structure of the complex can be compared with values of 6 Å for B-DNA (narrow minor groove) and 11 Å for A-DNA (wide minor groove). The mithramycin dimer cannot be accommodated in a narrow minor groove, and hence the DNA undergoes a conformational transition to form an intermediate-width minor groove on complex formation.

The extent of X-displacement of base pairs from the helix axis is quite distinct for B-DNA (–0.7 Å), where the helix axis passes through the base pairs, and for A-DNA (–5.4 Å), where the base pairs are displaced from the helix axis, resulting in a cavity down the center of the helix. The X-displacement values for all base pairs are typical of B-DNA for the d(T-C-G-C-G-A) duplex in the complex (Table VIII).

The majority of the sugar puckers and glycosidic torsion angles in the complex are characteristic of B-DNA helices (Table VIII). One exception is the sugar of C4, where both the sugar pucker and the glycosidic torsion angle belong to the A family of helices. We also note an A type pucker for the C2 sugar in the refined RM-B structure (Table VIII) which is supported by some of the NOE data (strong base-to-H3′ NOE cross peak) but not by the coupling constant data in Figure 5. The sugar puckers of C2, G3, and G5 are defined solely by the NOE constraints in the refined structures. We are currently attempting to check these conclusions on the basis of coupling constant simulations.

We observe sequence-dependent variations in the helical twist and rise parameters along the d(T-C-G-C-G-A) duplex in the complex (Table VII). These results emphasize that the DNA helix is distorted away from both the B and the A family of helices in the Mg^{2+}-coordinated Mth dimer–d(T-C-G-C-G-A) complex, and these changes must reflect accommodation and optimization of the intermolecular interactions stabilizing complex formation.

We note that the phosphorus resonances are dispersed over a 2 ppm chemical shift range for the Mg^{2+}-coordinated Mth dimer–d(T-C-G-C-G-A) complex (Figure 1C), in contrast to a smaller 0.5 ppm chemical shift dispersion for unperturbed B-DNA helices. It is clear that the phosphates at G3-C4, C4-G5, and G5-A6 steps in the complex (Figure 7) have shifted to high field of the unperturbed –4.0 to –4.5 ppm spectral region. The origin of these phosphorus complexation shifts is not understood at this time since there are no pronounced structural perturbations in the torsion angles of the phosphate backbone at these steps in the relaxation matrix refined RM-B structure. However, there are no constraints to define the phosphate backbone in our computations, and hence we cannot rule out alternate backbone alignments.

Mg^{2+}-Coordinated Mithramycin Dimer in the Complex. Several novel features associated with the relative alignment of the drug monomers to form the Mg^{2+}-coordinated mithramycin dimer in the complex with the d(T-C-G-C-G-A) duplex are evaluated below. We introduced nonexperimental constraints (see Materials and Methods) that maintained the O^9–Mg–O^9 angle at a value of 180° during the refinement process since this coordination geometry was observed in the crystal structure of the related Mg^{2+}-coordinated chromomycin dimer–DNA complex (C. Ogata, X. Gao, and W. Hendrickson, personal communication). The Mg^{2+} is most likely octahedrally coordinated with the O^9 atoms adopting apical positions (O^9–Mg–O^9 angle of 180°) and the O^1 atoms adopting adjacent in-plane orientations (O^1–Mg–O^1 angle of 80.4°) in the relaxation matrix refined RM-B structure (Table X and Figure 11). The two remaining octahedral coordination sites are likely to be occupied by bound waters at adjacent in-plane orientations similar to what was first established in the X-ray structure of the Mg^{2+}-coordinated chromomycin dimer–DNA complex (C. Ogata, X. Gao, and W. Hendrickson, personal communication). Since there are no constraints involving either the Mg^{2+} or the coordinated oxygens (O^9 and

O^1) with nearby protons, the coordination is solely determined by proton–proton constraints in the remainder of the complex during the refinement process.

Sequence-Specific Intermolecular Hydrogen-Bonding Interactions. The relaxation matrix refined RM-B structure of the Mg^{2+}-coordinated Mth dimer–d(T-C-G-C-G-A) complex identifies those elements that contribute to the base- and sequence-specific recognition of the DNA helix. The pair of symmetrical intermolecular hydrogen bonds between the donor amino protons of G3 and the acceptor phenolic hydroxyl O^8 oxygens on the hydrophilic edge of the aglycon explain the base specificity for (G-C)·(G-C) steps and minor groove recognition. The increase in helical twist and rise at the central (G3-C4)·(G3-C4) step (Table VII) and C3′-*endo* pucker formation at C4 (Table VIII) on complex formation which accompanies the widening of the minor groove most likely reflect conformational realignments necessary to maximize the intermolecular interactions in this binding segment of the complex.

Additional Hydrogen-Bonding Interactions. A second set of intermolecular hydrogen-bonding interactions contribute to the minor groove recognition of the DNA helix by the bound mithramycin dimer. These relate to the E sugar which is positioned with its hydrophilic OH-3 and OH-4 groups directed toward the floor of the minor groove between the T1·A6 and C2·G5 base pairs of the duplex in the complex. The hydroxyl protons donate hydrogen bonds to the guanine N^3 and cytidine O^2 atoms lining the minor groove edge of the C2·G5 base pair in the RM-B structure of the complex (Table XI). The OH-3 and OH-4 hydroxyls on the E sugar can function as hydrogen bond donors or acceptors to acceptors or donors on the minor groove edge of the DNA helix. This would reduce the recognition specificity at the flanking steps and account for Mth dimer binding to both (C-G-C-G) and (G-G-C-C) segments.

The OH-3′ and OH-4′ hydroxyl protons on the hydrophilic side chains can potentially form nonspecific hydrogen bonds with the backbone phosphates of the DNA. Indeed, in the relaxation matrix refined RM-B structure the OH-4′ group donates a hydrogen bond to the phosphate oxygen at the C4-G5 step in the complex (Table XI).

Aglycon–DNA Minor Groove Interactions. The aglycon of the mithramycin dimer participates in two types of intermolecular interactions that stabilize the complex. We have already discussed the intermolecular hydrogen bonds involving the phenolic hydroxyl O^8 oxygens that contribute to the sequence specificity of complex formation. The other interaction is of van der Waals type where the aglycon of each monomer is sandwiched between the C-D saccharide segments of its partner monomer and the sugar–phosphate backbone centered about the G3-C4 step (Figure 12). Indeed, the sugar ring of C4 stacks over the aromatic ring of the aglycon (Figure 12), explaining the upfield shifts at all the C4 sugar protons, including the large upfield shifts at the H4′ proton of C4 in the complex (Table I). The aglycon is partially buried in the complex with its hydrophobic edge (H5, H10, and H4 methylene protons) exposed to solvent.

Saccharide–DNA Minor Groove Interactions. A range of saccharide–DNA interactions are detected between the mithramycin dimer and the minor groove of the duplex. The C-D saccharide segment interacts edgewise in the antiparallel alignment with the C4-G5 segment of individual strands of the duplex through hydrophobic contacts involving the H1, geminal H2, and H3 protons on both the C and the D sugar (Figure 12A).

By contrast, the E sugar is positioned face down in the floor of the minor groove and spans both strands of the duplex (Figure 12A). Both hydrogen-bonding (OH-3 and OH-4) and hydrophobic (H1, H2, and H5) intermolecular interactions involving the E sugar contribute stabilizing contacts at either end of the duplex.

The A-B disaccharide segment primarily interacts with the minor groove edge of the sugar–phosphate backbone in the vicinity of the G3 sugar in the relaxation matrix refined RM-B structure of the complex. The hydrophobic edge (H1, geminal H2, and H3 protons) of the A sugar is directed toward the DNA backbone in the complex (Figure 13B). The partial wrapping of its DNA target site by the A-B disaccharide segment (Figure 13) may weakly clamp the mithramycin dimer and prevent its sliding along the minor groove of the helix.

The side-by-side antiparallel alignment of monomers in the Mg^{2+}-coordinated mithramycin dimer results in monomer-strand interactions in the central segment of the complex. Thus, the aglycon, the A-B disaccharide, the C-D disaccharide, and the hydrophilic side chain of each mithramycin monomer span the G3-C4-G5 segment of the interacting DNA strand in the complex (Figure 10). Only the terminal E sugar spans the (T1-C2)·(G5-A6) base pairs on both strands of the duplex. The net consequence of these intermolecular interactions is that the right-handed Mg^{2+}-coordinated mithramycin dimer spans a six-base-pair DNA segment extending outwards from the central (G-C)·(G-C) sequence-specific binding site (Figure 10).

Relaxation Matrix versus Distance-Restrained Refinement. Relaxation matrix refinement is driven by the gradient of the relaxation matrix with respect to all proton coordinates. Relaxation matrix refinement should correct for the errors in the distance estimation which are inherent in the ISPA (isolated spin pair approximation) approach, in which only direct interactions are taken into account and the contributions of spin diffusion interactions to the NOE intensity are ignored. Moreover, after relaxation refinement the agreement of the structure with experimental data can be quantified. When the distance-refined DR-A and DR-B structures (root mean square deviation = 1.44 Å) are compared to the relaxation matrix refined RM-A and RM-B structures (root mean square deviation = 1.06 Å), we observe that buckling at the terminal base pairs is reduced. The resulting back-calculated spectra also show that the agreement with experimental spectra improves with relaxation matrix refinement.

Comparison between Relaxation Matrix Refined RM-A and RM-B Structures. A stereoview of the superpositioned relaxation matrix refined structures RM-A and RM-B is shown in Figure S6 (supplementary material). The root mean square deviation between all atoms in RM-A and RM-B structures is 1.06 Å, compared to 3.20 Å in the starting Init-A and Init-B structures. For clarity, the superpositioned mithramycin dimer segments from the RM-A and RM-B structures are shown in Figure 9B. The mithramycin dimer in both refined structures exhibits a similar extended conformation. Further, the angle between the two chromophores is similar, as is the coordination geometry to the divalent cation. By contrast, the hydrophilic side chain and the B sugar are less precisely defined in our refined structures, reflected by the limited number of constraints in these segments. Two views of the superpositioned DNA segments from the RM-A and RM-B structures are shown in Figure 9A. The DNA groove widths are similar, as are the helical twist and rise parameters at individual steps in the RM-A and RM-B refined structures (Tables VII and SIII). Moreover, the X-displacement values for all the base

pairs are similar in the refined structures (Tables VIII and SIV). We detect differences in the backbone torsion angles at the T1-C2 step of the DNA segments in the RM-A and RM-B refined structures (Figure 9A), and this observation most likely reflects the limited number of distance constraints involving the terminal T1 residue.

A superposition of eight coordinate sets taken at 0.5-ps intervals from 1 to 2.5 ps of room temperature dynamics during relaxation matrix refinement starting from distance-refined structures DR-A and DR-B is plotted in Figure S7 (supplementary material). The corresponding root mean square deviations between these eight coordinate sets are listed in Table SV. These results establish that the relaxation matrix refined structures of the Mg^{2+}-coordinated mithramycin dimer–d(T-C-G-C-G-A) complex are well defined except for the hydrophilic side chain and B sugar on the drug and the T1-C2 step on the DNA.

Comparison of Chromomycin Dimer and Mithramycin Dimer Complexes with DNA. We previously reported NMR studies on complexes formed between Mg^{2+}-coordinated chromomycin dimer and the d(T-T-G-G-C-C-A-A) (Gao & Patel, 1989) and d(A-A-G-G-C-C-T-T) (Gao & Patel, 1990) self-complementary octanucleotide duplexes, including a relaxation matrix refinement of the latter complex (Gao et al., 1992). Our attempts to generate the Mg^{2+}-coordinated mithramycin dimer complexes with the same octanucleotide duplexes resulted in the generation of a mixture of two structures in equilibrium for both sequences. Thus, the mithramycin dimer binds with reduced sequence specificity, and hence we focused on complexation studies at the hexanucleotide duplex level. We have generated and characterized Mg^{2+}-coordinated mithramycin dimer complexes with the d(T-G-G-C-C-A) and d(T-C-G-C-G-A) self-complementary duplexes in this paper and report on a relaxation matrix refinement of the latter complex.

There are similarities at the global level, and some differences at the local level, between the solution structures of the Mg^{2+}-coordinated Chr dimer–d(A-A-G-G-C-C-T-T) complex (Gao et al., 1992) and the Mg^{2+}-coordinated Mth dimer–d(T-C-G-C-G-A) complex (this study). The same principles are used by both drugs to form divalent cation coordinated dimers, including the geometry at the coordination site, the alignment of the saccharide chains, and the aglycon–saccharide interactions. Both drug dimers bind to the minor groove of DNA centered about the central (G-C)·(G-C) step with the same symmetry-related aglycon phenolic O^8 hydroxyl–guanine NH_2 intermolecular hydrogen bonds. The C-D-E trisaccharide segments are positioned in the minor groove and are directed in an extended conformation toward either end of the duplex in the complexes. Further, the C-D saccharide segment shares the minor groove with its partner aglycon, while the E sugar lies in the floor of the minor groove in both complexes. Similar intermolecular contacts between the A-B disaccharide and the sugar–phosphate backbone are also detected in both complexes.

We wish to emphasize two important differences that have emerged from our studies on Chr dimer–DNA and Mth dimer–DNA complexes. One difference relates to the conformation of the tetranucleotide segment centered about the (G-C)·(G-C) central binding site in the complex. All four residues in the central tetranucleotide segment adopted A-helix sugar puckers and glycosidic torsion angles in the Chr dimer–DNA complex (Gao et al., 1992), while only the central cytosine residue in the central tetranucleotide segment adopted A-sugar puckers and glycosidic torsion angles in the Mth dimer–DNA complex (this study). The tendency toward an A-helix-like conformation for the entire central tetranucleotide segment in the Chr dimer–DNA complex but not in the Mth dimer–DNA complex appears to correlate with the chromomycin dimer being more hydrophobic (fewer hydroxyl functionalities on the sugar rings) than the mithramycin dimer. Despite this difference, the minor groove about the central tetranucleotide segment was wider and shallower to accommodate the drug dimers in both complexes.

The second difference relates to the interaction of the E sugars with the floor of the minor groove at a dinucleotide duplex segment one base pair removed in either direction from the center of symmetry of the complex. The E-sugar face containing the H1, H2e, OH-3, H4, and CH_3 groups interacts with the minor groove edge in the Chr dimer–DNA complex (Gao et al., 1992), while the E-sugar face containing the H1, H2e, OH-3, OH-4, and H5 groups interacts with the minor groove edge in the Mth dimer–DNA complex (this study). Thus, the interacting E sugar is more hydrophilic in the mithramycin dimer case since it has an additional OH group and lacks a CH_3 group relative to the chromomycin dimer. The hydrogen-bonding potential of the additional hydroxyl group at position 4 and replacement of the CH_3 by a hydrogen atom at position 5 on the E sugar most likely explain the reduced sequence specificity of the mithramycin dimer for sequences flanking the central (G-C)·(G-C) step in the complex.

ACKNOWLEDGMENT

We wish to thank Drs. Karen Greene, David Live, and R. Hosur for assistance in the early stages of this research and Drs. Craig Ogata, Xiaolian Gao, and William I. Weis for advice and discussions.

SUPPLEMENTARY MATERIAL AVAILABLE

Five tables listing proton complexation shifts (Table SI), carbon chemical shifts (Table SII), helical parameters in the RM-A refined structure (Tables SIII and SIV), and root mean square deviations between coordinate sets from the room temperature dynamics trajectory for the mithramycin dimer–d(T-C-G-C-G-A) complex (Table SV), and seven figures showing proton NMR spectra (Figure S1), NOE and coupling connectivities (Figure S2), and proton–phosphorus correlation for the mithramycin dimer–d(T-G-G-C-C-A) complex (Figure S3) and comparison between expanded experimental and calculated NOESY stacked plots (Figure S4), Init-A and Init-B starting structures (Figure S5), superpositioned RM-A and RM-B relaxation matrix refined structures (Figure S6), and superpositioned coordinate sets from room temperature dynamics trajectory for the mithramycin dimer–d(T-C-G-C-G-A) complex (Figure S7) (14 pages). Ordering information is given on any current masthead page.

REFERENCES

Altona, C., Haasnoot, C. A. G. (1980) *Org. Magn. Reson. 13*, 417–429.

Bakhaeva, G. P., Berlin, Yu. A., Boldyreva, E. F., Chuprunova, O. A., Kolosov, M. N., Soifer, V. S., Vasiljeva, T. E., & Yartseva, I. V. (1968) *Tetrahedron Lett. 32*, 3595–3598.

Banville, D. L., Keniry, M. A., Kam, M., & Shafer, R. H. (1990a) *Biochemistry 29*, 6521–6534.

Banville, D. L., Keniry, M. A., & Shafer, R. H. (1990b) *Biochemistry 29*, 9294–9304.

Berlin, Yu. A., Esipov, S. E., Kolosov, M. N., Shemyakin, M., & Tanaka, K. (1966) *Tetrahedron Lett. 15*, 1643–1647.

Berman, E., Brown, S. C., James, T. L., & Shafer, R. H. (1985) *Biochemistry 24*, 6887–6893.
Brady, J., Ha, S. N., Giammona, A., & Field, M. (1988) *Carbohydr. Res. 180*, 207–221.
Brooks, B. R., Bruccoleri, R. E., Olafson, B. D., States, D. J., Swaminathan, S., & Karplus, M. (1983) *J. Comput. Chem. 4*, 187–217.
Cerami, A., Reich, E., Ward, D. C., & Goldberg, I. H. (1967) *Proc. Natl. Acad. Sci. U.S.A. 57*, 1036–1042.
Cons, B. M., & Fox, K. R. (1989a) *Nucleic Acids Res. 17*, 8695–8714.
Cons, B. M., & Fox, K. R. (1989b) *Nucleic Acids Res. 17*, 5447–5429.
Cons, B. M., & Fox, K. R. (1990) *FEBS Lett. 264*, 100–104.
Cons, B. M., & Fox, K. R. (1991) *Biochemistry 30*, 6314–6321.
Elias, E. G., & Evans, J. T. (1972) *J. Bone Joint Surg. 54A*, 1730–1736.
Fox, K., & Howarth, N. R. (1985) *Nucleic Acids Res. 13*, 8695–8714.
Gao, X., & Patel, D. J. (1989a) *Biochemistry 28*, 751–762.
Gao, X., & Patel, D. J. (1989b) *Q. Rev. Biophys. 22*, 93–138.
Gao, X., & Patel, D. J. (1990) *Biochemistry 29*, 10940–10956.
Gao, X., Mirau, P., & Patel, D. J. (1991) *J. Mol. Biol. 222*, 259–279.
Grundy, W. E., Goldstein, A. W., Rickher, C. J., Hares, M. E., Varren, H. G., Jr., & Sylvester, J. C. (1953) *Antibiot. Chemother. (Washington, D.C.) 3*, 1215.
Hare, D. R., Wemmer, D. E., Chou, S. H., Drobny, G., & Reid, B. R. (1983) *J. Mol. Biol. 171*, 319–336.
Keniry, M. A., Brown, S. C., Berman, E., & Shafer, R. H. (1987) *Biochemistry 26*, 1058–1067.
Kennedy, B. J. (1966) *Cancer Res. 26*, 36–39.
Kennedy, B. J., Yarbo, J. W., Kickertz, V., & Sandberg Wollheim, M. (1968) *Cancer Res. 28*, 91–97.
Lavery, R., & Sklenar, H. (1988) *J. Biomol. Struct. Dyn. 6*, 63–91.
Leroy, J. L., Gao, X., Gueron, M., & Patel, D. J. (1991) *Biochemistry 30*, 5653–5661.
Marion, D., Ikura, M., & Bax, A. (1989) *J. Magn. Reson. 84*, 425–430.
Miller, D. M., Sanchez, J. D., Ray, R., Snyder, R. C., Blume, S., Shreshta, K., Bailey, A., Bounelis, P., Thomas, S., Pezzementi, M., Rigsby, D., Hunter, D., & Koller, C. A. (1989) *Cancer Res. 3*, 119–135.
Miyamoto, M., Kawamatsu, Y., Kawashima, K., Shinohara, M., Tanaka, K., Tatsuoka, S., & Nakanishi, K. (1967) *Tetrahedron 23*, 421.
Nilges, M., Hazabettl, J., Brunger, A. T., & Holak, T. A. (1991) *J. Mol. Biol. 219*, 499–510.
Patel, D. J. (1976) *Biopolymers 15*, 533–558.
Philip, J. E., & Schenck, J. R. (1953) *Antibiot. Chemother. (Washington, D.C.) 3*, 1218.
Plateau, P., & Gueron, M. (1982) *J. Am. Chem. Soc. 104*, 7310–7311.
Ramakrishna, N., Miller, D. M., & Sakai, T. T. (1990) *J. Antibiot. 43*, 1543–1552.
Ray, R., Snyder, R., Thomas, S., Koller, C. A., & Miller, D. (1989) *J. Clin. Invest. 83*, 2003–2007.
Shapiro, L., Nilges, M., & Eriksson, M. (1992) *Acta Chem. Scand. 47*, 43–56.
Sklenar, V., & Bax, A. (1987) *J. Am. Chem. Soc. 109*, 7525–7526.
Stankus, A., Goodisman, J., & Dabrowiak, J. C. (1992) *Biochemistry 31*, 9310–9318.
States, D. J., Haberkorn, R. A., & Reuben, D. J. (1982) *J. Magn. Reson. 48*, 286–292.
Theim, J., & Meyer, B. (1981) *Tetrahedron 37*, 551–558.
Van Dyke, M. W., & Dervan, P. B. (1983) *Biochemistry 22*, 2373–2377.
Wakasaki, G., Uchino, H., Nakamura, T., Sotobayashi, H., Shivakawa, S., Adachi, A., & Sakurai, M. (1963) *Nature 198*, 385.
Ward, D. C., Reich, E., & Goldberg, I. H. (1965) *Science 149*, 1259.
Yip, P., & Case, D. A. (1989) *J. Magn. Reson. 83*, 643–648.